

1
2
3
4
5
6
7
8
9
10
11
12
13
14
15
16
17
18
19
20
21
22
23
24
25

**Aerosol Optical Properties Derived from the DRAGON-NE Asia campaign, and
Implications for Single Channel Algorithm to Retrieve Aerosol Optical Depth in
spring from Meteorological Imager (MI) On-board Communication, Ocean and
Meteorological Satellite (COMS)**

Mijin Kim¹, Jhoon Kim^{1,*}, Ukkyo Jeong¹, Woogyung Kim¹,
Brent Holben², Thomas F. Eck^{2,3}, Jae Hyun Lim⁴, Chang Keun Song⁴, Sukjo Lee^{4,+}

¹ Department of Atmosphere Sciences/IEAA BK 21 plus, Yonsei University, Seoul,
Korea

² NASA Goddard Space Flight Center, Greenbelt, MD, U.S.A.

³ Universites Space Research Association, Columbia, MD, USA

⁴ National Institute of Environmental Research(NIER), Inchon, Korea

⁺ Now at Asia Center for Air Pollution Research(ACAP), Niigata-shi, Japan

*Corresponding author.

Institute of Earth, Astronomy, and Atmosphere, Brain Korea 21 Plus Program,

Department of Atmospheric Sciences, Yonsei University, Seoul, Republic of Korea

Tel.: +82-2-2123-5682, Fax: +82-2-365-5163

E-mail address: jkim2@yonsei.ac.kr (Jhoon Kim)

26 **Abstract**

27

28 Aerosol model optimized for North East Asia is updated with the inversion data from
29 the Distributed Regional Aerosol Gridded Observation Networks (DRAGON)-
30 Northeast (NE) Asia campaign during spring from March to May in 2012. This
31 updated aerosol model was then applied to a single visible channel algorithm to
32 retrieve aerosol optical depth (AOD) from a Meteorological Imager (MI) on-board the
33 geostationary meteorological satellite, Communication Ocean and Meteorological
34 Satellite (COMS). This model plays an important role in retrieving accurate aerosol
35 optical depth (AOD) from a single visible channel measurement. For the single
36 channel retrieval, sensitivity tests showed that perturbations by 4 % (0.926 ± 0.04) in
37 the assumed single scattering albedo (SSA) can result in the retrieval error in AOD by
38 over 20%. Since the measured reflectance at top-of-atmosphere depends on both AOD
39 and SSA, the overestimation of assumed SSA in aerosol model leads to an
40 underestimation of AOD. Based on the AErosol RObotic NETwork (AERONET)
41 inversion datasets obtained over East Asia before 2011, seasonally analyzed AOPs
42 was categorized by SSAs at 675 nm of 0.92 ± 0.035 for spring (March, April, and May).
43 After the DRAGON-NE Asia 2012, the SSA during spring showed a slight increase to
44 0.93 ± 0.035 . In terms of the volume size distribution, the mode radius of coarse
45 particles were increased from 2.08 ± 0.40 to 2.14 ± 0.40 . While the original aerosol
46 model consists of volume size distribution and refractive indices obtained before 2011,
47 the new model is constructed by using total dataset after the DRAGON-NE Asia
48 campaign. The large volume of dataset in high spatial resolution from this intensive
49 campaign can be used to improve the representative aerosol model for East Asia.

50 Accordingly, the 'new' AOD datasets retrieved from a single channel algorithm,
51 which uses a pre-calculated look-up table (LUT) with the new aerosol model, show an
52 improved correlation with the measured AOD during the DRAGON-NE Asia
53 campaign. The correlation between the new AOD and AERONET value shows
54 regression slope of 1.00, while the comparison of the 'original AOD' retrieved using
55 the original aerosol model shows the slope of 1.08. The change of y-offset is not
56 significant, and the correlation coefficients for the comparisons of the original and
57 new AOD are 0.87 and 0.85, respectively. The tendency of the original aerosol model
58 to overestimate the retrieved AOD is significantly improved by using the SSA values
59 in addition to size distribution and refractive index obtained using the new model.

60

61 Keywords: Aerosol optical depth, Single channel algorithm, DRAGON-NE Asia 2012

62

63

64 **1. Introduction**

65

66 An understanding of global aerosol distribution and its optical characteristics is
67 important not only for predictions related to climate change, but also for monitoring
68 the effects of changing air quality on human health. It is widely accepted that aerosol
69 has both direct and indirect effects on the Earth radiation budget (IPCC, 2013).
70 Aerosols are also linked to respiratory illness (e.g. Pope and Dockery, 2006) and
71 meningitis epidemics (e.g. Deroubaix et al., 2013). Since the global aerosol
72 distribution shows high spatial and temporal variability, many studies have developed
73 aerosol retrieval algorithms utilizing both low earth orbit (LEO) satellite
74 measurements (Hsu et al., 2004; Kim et al., 2007; Torres et al., 2007; Kahn et al.,
75 2010; Lyapustin et al., 2011b; von Hoyningen-Huene et al., 2011; Wong et al., 2010;
76 Bevan et al., 2012; Sayer et al., 2012; Levy et al., 2013) and geostationary orbit (GEO)
77 satellite measurements (Knapp et al., 2002, 2005; Wang et al., 2003; Urm and Sohn,
78 2005; Yoon et al., 2007; Kim et al., 2008; Lee et al., 2010b; Zhang et al., 2011; Kim
79 et al., 2014). These studies have typically adopted an inversion approach, using a pre-
80 calculated look-up table (LUT) based on assumed aerosol optical properties (AOPs)
81 to retrieve aerosol information from the measured visible reflectance at the top of the
82 atmosphere. In this method, the accurate estimation of surface reflectance and
83 assumption of optimized aerosol optical type are key to retrieve accurate aerosol
84 information. The surface information was taken account by using single view
85 algorithm based on multi-channel algorithm with certain assumption (e.g. Levy et al.,
86 2007b), or by using multiple view algorithms for the Multi-angle Advanced Along-
87 Track Scanning Radiometer (AATSR) (Grey et al., 2006) or the Polarization and
88 Directionality of Earth Reflectances (POLDER) sensor (Waquet et al., 2009)

89 measurement. Under conditions of low aerosol optical depth (AOD), the estimation of
90 surface reflectance is most crucial to retrieve accurate AOD, while assumptions about
91 the type of aerosol are more significant for cases with higher AOD. A variation in
92 single scattering albedo (SSA) of $\pm 3\%$ (based on a reference value of 0.90) results in a
93 10% error for moderate AOD ($\tau = 0.5$ at $0.67 \mu\text{m}$) and a 32% error for large AODs (τ
94 $= 1.5$) (Zhang et al., 2001). Lee et al. (2012) used a tri-axial ellipsoidal database of
95 dust (Yang et al., 2007) and inversion data from the Aerosol Robotic Network
96 (AERONET) to greatly improve the AOD retrieved using the MODIS dark target
97 algorithm with regards to its Pearson coefficient (from 0.92 to 0.93), regression slope
98 (from 0.85 to 0.99), and the percentage of data within an expected error bound (from
99 62% to 64%).

100 Ground-based measurements are essential to the construction of a well-defined
101 aerosol model to calculate LUT. Aerosol observations from ground-based sun/sky
102 radiometer measurements, such as the AERONET, provide accurate global and local
103 AOPs, including AOD and particle characteristics (Duvobik et al., 2000; Holben et al.,
104 1998). Numerous aerosol models for satellite aerosol algorithms have been based on
105 the AERONET datasets (e.g. Sayer et al., 2014), and these models can be further
106 improved by using AOPs obtained from intensive field campaigns in high spatial
107 resolution (e.g. Huebert et al., 2003; Nakajima et al., 2007). Recently, the Distributed
108 Regional Aerosol Gridded Observation Networks (DRAGON)-Northeast (NE) Asia
109 2012 campaign over South Korea and Japan, during spring from March to May 2012,
110 provided a valuable insight into the characteristics of aerosol over metropolitan areas
111 ([http://aeronet.gsfc.nasa.gov/new_web/DRAGONAsia_2012_Japan_South_Korea.ht](http://aeronet.gsfc.nasa.gov/new_web/DRAGONAsia_2012_Japan_South_Korea.html)
112 [ml](http://aeronet.gsfc.nasa.gov/new_web/DRAGONAsia_2012_Japan_South_Korea.html)). The campaign studied aerosol characteristics over known polluted areas affected
113 by diverse aerosol sources such as urban pollutants and transported dust. In addition,

114 the high-spatial resolution data from the campaign were used to validate the satellite
115 aerosol algorithms covering the same region.

116 To investigate the role of the mesoscale network of ground-based aerosol
117 measurements in the satellite-based AOD retrieval, an aerosol retrieval algorithm
118 based on the inversion method is tested in this study. By using a single-visible
119 measurement of Meteorological Imager (MI) on-board the Communication, Ocean,
120 and Meteorological Satellite (COMS), an AOD retrieval algorithm was developed by
121 Kim et al. (2014), and provides valuable results regarding aerosol distribution and
122 transport. Since the algorithm cannot detect temporal and spatial variation of AOPs,
123 the single type of assumed, optimized aerosol model was used as previous studies (e.g.
124 Knapp et al., 2002; Yoon, 2006; Yoon et al., 2007; Wang et al., 2003). In this regard,
125 the representative aerosol model is important to reduce the uncertainty in AOD
126 retrieval. Here, the aerosol model is newly analysed from the previous study (Kim et
127 al., 2014) by using extended dataset after the DRAGON-NE Asia campaign. The
128 campaign which focuses on the monitoring of aerosol properties over Korea and
129 Japan can provide details of aerosol distribution, and contribute to accumulate the
130 data set. The new aerosol model applied to the single channel algorithm, and the
131 retrieved AODs are compared with directly measured values from the DRAGON-NE
132 Asia campaign.

133 The single channel algorithm used in this study is similar in nature to that described
134 by Kim et al. (2014), which improved the basic single channel algorithm by applying
135 the critical reflectance method and background AOD (BAOD) correction. To consider
136 the importance of the aerosol type selection, the algorithm applied the critical
137 reflectance method (Fraser and Kaufman, 1985) to determine the SSA for each
138 measured scene over urban areas. Meanwhile, the BAOD, representing the persistent

139 concentration of aerosol even in the clearest air condition, was estimated by finding
140 the minimum AOD among the long-term measurement. Since the algorithm estimated
141 surface reflectance based on the minimum reflectance method, underestimation or
142 neglect of the BAOD results in the overestimation of the surface reflectance, and thus
143 leads to the underestimation of AOD (Knapp et al., 2002; Yoon, 2006). The
144 correction for BAOD to the surface reflectance showed significant effects in the Kim
145 et al. (2014), and is also considered here, whereas the critical reflectance method is
146 not adopted to evaluate the effects of assumed aerosol property to the AOD retrieval.
147 Though the accuracy of AOD retrieved from the single channel algorithm is limited
148 because of the limitation in type detection, the products obtained from GEO
149 measurement has an advantage of continuous monitoring of aerosol emission and
150 transport from source region in high temporal resolution. The continuous monitoring
151 is expected to improve the capabilities to predict ambient aerosol properties (e.g.
152 Saide et al., 2014; Park et al., 2014).

153 The datasets used in this study are summarized in section 2, and details of the single
154 channel algorithm and its results are described in section 3. Modifications to the
155 aerosol model using data from the DRAGON-Asia campaign, and their effects on
156 subsequent retrievals, are outlined in section 4.

157

158 **2. Data**

159

160 **2.1. DRAGON-NE Asia Campaign**

161

162 The AERONET, a network of globally distributed ground-based sun photometers, is
163 widely used to understand global AOPs and to validate satellite-based aerosol

164 products. The AERONET sun photometer measurements of direct solar radiation
165 provide accurate measurements of AOD (~ 0.01 in the visible and near-infrared and
166 ~ 0.02 in the UV) under cloud-free conditions (Eck et al., 1999; Holben et al., 1998;
167 Holben et al., 2001), and sky radiance measurements in an almucantar scenario can be
168 inverted to calculate AOPs such as size distribution, single scattering albedo, phase
169 functions, and the complex index of refraction (Dubovik and King, 2000; Dubovik et
170 al., 2000; Dubovik et al., 2002).

171 During the DRAGON-NE Asia campaign in 2012, 20 Cimel sun-sky radiometer
172 instruments were deployed in Seoul, as well as in eastern and western parts of South
173 Korea. In Japan, about 20 instruments were deployed in Osaka, West Japan and
174 Fukushima valley. The distribution of DRAGON-Korea and -Japan sites is shown in
175 Figure 1, along with the number of AOD data provided in level 2.0 (cloud screened
176 and quality assured; Smirnov et al., 2000) direct products during the campaign. Those
177 deployed sun photometers provided the high spatial-resolution information to address
178 characteristics of mega-city aerosol. Figure 2 shows average and standard deviation
179 for each of AOD (500 nm) and Ångström Exponent (AE, 440 – 870 nm) measured
180 during the campaign. In Figure 2(a), the average AOD ranged between 0.23 and 0.52,
181 and showed a decreasing behavior towards southeast. The maximum value of 0.52
182 was found at two sites in Fukue (128.68°E, 32.75°N) and Sanggye (127.07°E,
183 37.66°N), while the minimum value of 0.23 was found at Kohriyama site (140.38°E,
184 37.36°N). In terms of local average, the mean AOD of 0.43 in Seoul was higher than
185 the value of 0.30 in Osaka. Similarly, the standard deviation of AOD in Figure 2(b)
186 was low in the eastern part of Korea. While the standard deviation varied between
187 0.22 and 0.31 in Seoul, the values in Japan were between 0.11 and 0.16. The regional
188 difference was figured out also in terms of AE in Figure 2(c). The respective average

189 AE of 1.20 and 1.27 in Seoul and Osaka represents that the particle size in Seoul is
190 larger than that of Osaka, in general. The spatial distributions of AOD and AE can be
191 related closely with transport of aerosol in East Asia during winter and spring (Park et
192 al., 2014).

193 In this study, the extensive AERONET inversion data (level 2.0 daily products) over
194 East Asia (20°N–50°N, 95°E–145°E) were used to analyse optimized AOPs; the
195 retrieved volume size distribution and complex refractive indices, which are utilized
196 to compute the spectral SSA. Duvobik et al. (2000) recommended that the quality of
197 refractive index and SSA becomes reliable when the AOD (440 nm) is higher than 0.4
198 and solar zenith angle is higher than 45 °. To avoid insufficient data points for low
199 AOD case, the daily averaged product were applied. Level 2.0 AOD datasets
200 measured for the DRAGON-NE Asia 2012 campaign with more than 50 data points
201 were used to validate the retrieval results. The AERONET sites used, including the
202 campaign sites, are listed in Table 1, along with the period of the inversion products.
203 The campaign sites are numbered, and sites indicated by bold character represent the
204 validation site selected randomly to test the consistency of the retrieval accuracy. The
205 inversion products obtained at those validation sites were not applied to analyse the
206 aerosol model, but direct AOD products were used to validate the algorithm. While a
207 total of 12,126 inversion datasets from 1999 to 2012 were compiled, 84,091 AOD
208 datasets at 39 sites in spring of 2012 were applied from the campaign.

209

210 **2.2. COMS Meteorological Imager**

211

212 A multi-purpose geostationary satellite, COMS, designed to orbit at a longitude of
213 128.2°E, was launched on June 27, 2010 by the Korean government. The satellite

214 performs meteorological and ocean monitoring by using the MI and Geostationary
215 Ocean Color Imager (GOCI) instruments. The MI measures the single visible
216 reflectance (0.55–0.80 μm) at a 1 km spatial resolution, and the brightness
217 temperature (BT) at four IR wavelengths at a 4 km spatial and 30 min temporal
218 resolution. The four IR channels cover spectral ranges of 10.3–11.3 (IR1), 11.5–12.5
219 (IR2), 6.5–7.0 (IR3), and 3.5–4.0 μm (IR4). The MI can cover a full disk from its
220 equatorial position at 128.2°E, though this study focuses mainly on images from East
221 Asia. The MI measurement from the single visible and four IR channels are applied to
222 retrieve land and ocean surface temperature, incoming and outgoing radiance, and
223 atmospheric variables including aerosol, cloud properties, precipitable water, and
224 upper tropospheric humidity. The level2 products can be found from the National
225 Meteorological Satellite Center (<http://nmsc.kma.go.kr/html/homepage/ko/main.do>)
226 of Korea.

227

228 **2.3. MODIS AOD**

229

230 To estimate the BAOD distribution over East Asia over long period, an AOD product
231 at $10 \times 10 \text{ km}^2$ resolutions from the Moderate Resolution Imaging Spectroradiometer
232 (MODIS) was used (Collection 5.1; MYD04_Lv2.0). The AOD at 550 nm from a
233 dark target algorithm (Levy et al., 2007b, 2010; Remer et al., 2005) was interpolated
234 onto a grid of $0.25^\circ \times 0.25^\circ$ to find the minimum value for each area. Considering
235 spatial variation of BAOD, the MODIS product was applied to cover wider area over
236 long term, although satellite measurement has larger uncertainty than the ground-
237 based measurement. The expected error in the AOD product is $\pm(0.05 + 15\%)$, and

238 over 66% of the retrieved AODs from the MODIS algorithm lie within the error range,
239 with a correlation coefficient of 0.9 (Levy et al., 2010). Despite of the seasonal
240 variation of atmospheric condition over North East Asia, the seasonal variation of the
241 BAOD was not considered because of insufficient data points for winter and summer
242 depending on snow surface and summer monsoon. The uncertainty related with the
243 BAOD assumption will be discussed in section 3.5.

244

245 **3. Single channel algorithm**

246

247 The basic concept of the single channel algorithm suggested in Kim et al. (2014) lies
248 in the inversion of the TOA reflectance to AOD by using the sensitivity of the TOA
249 reflectance to AOD under the condition of fixed aerosol model, with known geometry
250 and retrieved surface reflectance. The sensitivities of the reflectance to each variable
251 are from a forward-model, RTM, assuming certain microphysical properties for the
252 aerosol. The results are compiled into a LUT, where the assumed characteristics of the
253 AOPs form the basis for the aerosol model. Generally, the LUT for a single channel
254 algorithm lists the calculated reflectance as a function of AOD, surface reflectance,
255 measurement geometry, and the assumed aerosol model. In this study, a dynamic
256 aerosol model was constructed using long-term AERONET inversion data to consider
257 changes in refractive index, the mode radius and the width (standard deviation) in the
258 volume size distribution with respect to the AOD. The volume size distribution
259 consists of two modes, fine and coarse, and both vary in accordance with assumed
260 AOD in the RTM simulation. In addition, the aerosol model was designed to include
261 the seasonal variation in AOPs, with a different LUT selected depending on the
262 season in which the measurement was taken. A flowchart of the AOD retrieval

263 algorithm for MI measurements is shown in Figure 3. To estimate surface reflectance,
264 the minimum reflectance method was applied under the assumption that the increase
265 in AOD makes a positive contribution to TOA reflectance over a dark surface. The
266 minimum TOA reflectance obtained from the previous 30-day measurement was
267 converted to surface reflectance, after correcting for scattering by atmospheric
268 molecules and for BAOD.

269

270 **3.1. Cloud masking**

271

272 The AOD was retrieved only for cloud-free pixels satisfying threshold tests of TOA
273 reflectance and brightness temperature (BT). The threshold of 0.35 for the TOA
274 reflectance at the visible channel separated bright cloud pixel, and the threshold of 5
275 K for the BT difference between the maximum BT for the previous 30 days and the
276 BT of the current pixel separated cold cloud pixel. The pixels which have BT lower
277 than 265 K were also masked out. Additionally, thresholds for BT differences
278 between IR1 and IR2, and IR1 and IR4 were taken from Frey et al. (2008). The
279 thresholds to distinguish cloud and aerosol pixel (IR1-IR2 BTD), and to detect low
280 level cloud (IR1-IR4 BTD) were adjusted as follows by trial and error. The positive
281 BTD between IR1 and IR2, and the largely negative BTD ($< -6\text{K}$) were found in
282 cloud pixel. Thus, the cloud masking procedure includes the following tests:

283

284 $\text{Visible reflectance} > 0.35$

285 $\text{IR1-IR2} > 0.5 \text{ K} \ \& \ \text{IR1} < 268 \text{ K}$

286 $\text{IR1-IR2} > 0.5 \text{ K} \ \& \ \text{IR1}_{\text{max}} - \text{IR1} > 5 \text{ K}$

287 $\text{IR1-IR2} > 1.5 \text{ K} \ \& \ \text{IR1-IR4} < -6 \text{ K for Ocean}$

288 $IR1-IR2 > 0.5 K$ & $IR1-IR4 < -10 K$ for Ocean

289 $IR1-IR2 > 1.5 K$ & $IR1-IR4 < -14 K$ for Land

290

291 **3.2. Surface reflectance and BAOD**

292

293 The BAOD represents a residual AOD value even in the clearest conditions; i.e. the
294 minimum AOD for each location. According to analyses of global AERONET direct
295 measurements, the minimum AOD over urban areas or near an aerosol source region
296 is non-zero due to the steady emission of aerosol (Kim et al., in preparation). An
297 underestimation of BAOD results in an underestimation of retrieved AOD. In an
298 environment of continuous development, population growth, and desertification, the
299 BAOD is not negligible, particularly over East Asia. Accordingly, Kim et al. (2014)
300 used the monthly BAOD obtained from AERONET direct measurements in Hong
301 Kong for AOD retrieval in the region. Subsequently, the BAOD was estimated from
302 the MODIS AOD product for 7 years from 2006 to 2012, and used here in order to
303 take advantage of the fine spatial resolution of the satellite measurements. The BAOD
304 ranged from 0.00 to 0.56, with an average value of 0.03 (Figure 4). Over ocean,
305 spatial variation of BAOD was not significant because the background aerosol is most
306 likely sea-salt with the median value of 0.022. Over land, however, the spatial
307 distribution of BAOD was related to surface type. While the median of BAOD over
308 land was 0.017, the values near metropolitan areas such as Beijing, Seoul, Tokyo, and
309 Hong Kong were generally higher than 0.1. Over the industrialized region located in
310 the lower reaches of the Yangtze River and near Hong Kong, the values even reached
311 over 0.30. Conversely, the region located far from the aerosol source showed low

312 BAODs. Overall, the BAOD map clearly reveals the most heavily polluted region as a
313 hotspot.

314 The surface reflectance was estimated from the minimum TOA reflectance, after
315 correcting for atmospheric and BAOD effects. For details of the atmospheric
316 correction, see Kim et al. (2014).

317

318 **3.3. Integration of Aerosol model**

319

320 The calculated TOA reflectance from RTM simulations is affected by the
321 concentration, particle size/shape and scattering properties of aerosol. Consequently,
322 an increase in the SSA of the particle correlates positively with TOA reflectance for
323 the same AOD. The use of a well-defined aerosol model to generate the LUT is
324 therefore crucial to obtain accurate AOD values from the inversion method. Although
325 spatial variation of the aerosol characteristics shown in Figure 2 was not taken into
326 account, a regionally integrated aerosol model over the area of interest suggest typical
327 properties from these areas, since the geostationary MI steadily observes the same
328 field of view from a fixed location. In this study, the aerosol models were obtained
329 from a seasonal average of AERONET inversion datasets over East Asia. There are
330 two groups of inversion datasets applied to examine the effect of the DRAGON-NE
331 Asia campaign on the retrieval accuracy of aerosol. The first datasets were compiled
332 from 18 AERONET sites from 1999 to 2010, with total 4898 data points as used by
333 Kim et al. (2014). This group was named as the ‘original’ dataset, where the name and
334 location of these sites are represented by italic type. The full list shown by normal
335 character in Table 1 summarizes the sites used to construct the ‘new’ data set as
336 described in Section 2.1.

337 The new group includes 40 additional AERONET sites and extends the measurement
338 period by up to 2 years (2011 ~ 2012) including the campaign. The greater quantity of
339 data, from the increased number of sites for the extended measurement periods,
340 allows us to optimize the aerosol model for the region of interest.

341 To compare the effects of the temporal extension and spatially more dense
342 measurements, the integrated AOPs for each case are presented in Table 2. In the
343 table, AOPs considered to calculate LUT for MAM (March, April, and May) season
344 were listed for each AOD bin in order of SSA, refractive index, effective radius and
345 standard deviation of volume size distribution, and the number of integrated data. To
346 consider the change in AOP with respect to AOD suggested by Levy et al. (2007), the
347 AOPs were categorized for six AOD bins. The bins are categorized by 0.0-0.3, 0.3-0.6,
348 0.6-1.0, 1.0-1.4, 1.4-1.8, and 1.8-3.0, and the median values of each AOD bin are
349 shown in Table 2. Though AERONET inversion data provide four spectral SSAs at
350 440, 675, 870, and 1020 nm, the values at 675 nm were analysed considering the
351 spectral range of MI visible channel. For the LUT calculation, however, wavelength
352 dependence of the refractive index was obtained from the AERONET retrieval and
353 applied. Based on the wavelength dependence, the AOD was retrieved at 550 nm. The
354 total average and standard deviation of the SSA for the ‘original’ group (Table 2(a))
355 was 0.92 and 0.035, respectively. The SSA ranged between 0.911 and 0.925 in order
356 of AOD. Accordingly, real part of the refractive index showed positive correlation
357 with the AOD. The increase of AOD caused the increase of effective radius and
358 standard deviation of fine mode size distribution, too. With the quality criteria of the
359 inversion products, the number of data points was significantly low for the low AOD
360 bin. The number of data was also decreased with the increasing AOD. In Table 2 (b),
361 the AOPs obtained from the temporally extended datasets from the same sites were

362 listed. A slight increase of the effective radius for coarse mode particle was found for
363 the low AOD cases in accordance with the increase of the number of data. When the
364 dataset from the DRAGON-NE Asia campaign, and a few additional sites in China
365 not included in the original study, were applied, all of AOD bins showed increased
366 SSA by more than 0.005, and the average value was 0.93 ± 0.035 . The larger dataset
367 resulted in SSA by about 1%, though the variation is lower than the standard
368 deviation of SSA. The increase in SSA may also be due to a temporal change in SSA
369 which was suggested in Lyapustin et al. (2011a). The previous study showed
370 increases in SSA in eastern China from 2000 to 2010 by about 0.02 at 470 nm. The
371 imaginary part of the refractive index was generally decreased, and the decrease was
372 more significant for low AOD condition than high AOD condition. Meanwhile, the
373 increasing effective radius of coarse particle was also found. Figure 5 shows the
374 volume size distribution analysed from the original (Figure 5a) and the new data
375 (Figure 5b) group for each AOD bin. In general, the coarse mode particles of a bi-
376 modal log-normal size distribution tend to dominate due to sporadic dust events [e.g.
377 Lee et al., 2010b]. With the increase in AOD, the mode radius of fine particles is
378 increased, while that of coarse particles is decreased [Levy et al., 2007a]. The
379 effective radius and standard deviation for fine and coarse mode were listed in Table
380 2(a) and (c).

381 Using aerosol models derived from both the original and new datasets, LUTs were
382 calculated by using the 6SV (Second Simulation of a Satellite Signal in the Solar
383 Spectrum–Vector) RTM (Vermote et al., 1997; Kotchenova et al., 2006; Kotchenova
384 and Vermote, 2007). In addition to measurement geometry (i.e. solar zenith angle,
385 viewing zenith angle, and relative azimuth angle), the surface reflectance, aerosol

386 model, and AOD were provided as input variables to calculate the LUTs. Surface
387 elevation was also included to increase the accuracy of Rayleigh scattering correction.
388 As mentioned above, the AOD is retrieved by comparing measured and calculated
389 TOA reflectance for a given set of measurement condition. The values in the LUTs
390 were linearly interpolated with the values in the neighbouring bins because the
391 calculation of TOA reflectance is performed as a function of several input variables.
392 To test the effects of the changes in aerosol models, the AODs were respectively
393 derived by using the original and the new LUTs.

394

395 **3.4. Sensitivity to assumed aerosol optical properties**

396

397 To estimate the accuracy of retrievals from the inversion of the single channel
398 algorithm, and to understand its sensitivity to uncertainty in the assumed SSA, a
399 reference test was performed. In this test, the TOA reflectance, was analysed within a
400 $\pm 4\%$ variation in SSA relative to the reference condition, from simulations using the
401 RTM for four different reference conditions of both AOD and SSA with assumed
402 geometries. The 4% variation covers the standard deviation of 0.035 for the integrated
403 SSA of 0.92 mentioned in section 3.3. In the simulation, the surface reflectance was
404 assumed to be 0.05 and 0.10, and the scattering angle was varied from 135.7° to 173.2°
405 with respect to the geostationary measurement conditions. The surface elevation was
406 at sea level, and cloud-free conditions were assumed. The retrieved AOD from the
407 simulated reflectance was then compared with the assumed reference AOD value.
408 Because the AOD was retrieved from the simulated TOA reflectance by assuming the
409 reference SSA, the $\pm 4\%$ variation in SSA cause an error in AOD. The results for the
410 comparison between the reference value and retrieved AODs for each simulated

411 reflectance are shown in Figure 6. The case with zero SSA error indicates that the
412 assumed SSA for the retrieval was the same as the reference SSA. In other cases, the
413 positive error in SSA indicates that the SSA used to calculate the LUT was
414 overestimated when compared with the reference value. The errors in AOD and SSA
415 were calculated as follows:

416

$$417 \quad \text{AOD error [\%]} = [(\text{retrieved AOD} - \text{reference AOD})/\text{reference AOD}] \cdot 100$$

418

$$419 \quad \text{SSA error [\%]} = [(\text{assumed SSA} - \text{reference SSA})/\text{reference SSA}] \cdot 100$$

420

421 Strong negative correlation was found between the errors in SSA and AOD. The error
422 in SSA was negatively correlated with error in AOD, and thus the overestimation of
423 SSA leads to an underestimation of AOD. In terms of the absolute value of AOD error,
424 the effects of the positive and negative errors in SSA are symmetric in general, though
425 the effect of the negative error in SSA is slightly greater. The effect of assumed errors
426 in SSA is more significant in scenarios with higher AOD. The SSA error of $\pm 3\%$
427 results in an AOD error of -18.70% (-0.03 , an absolute difference) and $+20.34\%$
428 ($+0.03$), respectively, when the reference AOD is 0.15 and the surface reflectance is
429 0.05. The range of error is increased when the reference AOD is higher, with retrieval
430 errors of -20.03% (-0.24) and $+23.31\%$ ($+0.28$) caused by a $\pm 3\%$ SSA error when the
431 reference AOD is 1.20.

432 The error in AOD also increases with the increase of assumed surface reflectance
433 relative to true reflectance. When the surface reflectance is increased from 0.05 to
434 0.10, the errors in the reference AOD of 0.15 ranged between -35% (-0.05) and 36%
435 ($+0.05$). The increase of effect of the SSA assumption was related with the one-to-one

436 correlation between the ‘critical reflectance’ and SSA reflectance (Castanho et al.,
437 2008; Fraser and Kaufman, 1985). Whereas the increase of aerosol contributes to the
438 increase of TOA reflectance over dark surface, the increase of AOD reduces the TOA
439 reflectance by shielding the upwelling reflectance from bright surface. There exist,
440 therefore, the surface reflectance at which the positive and negative contributions of
441 aerosol to the TOA reflectance are cancelled out, then the surface reflectance is
442 known as the critical reflectance. In consideration of the positive relationship between
443 the critical reflectance and SSA, the sensitivity to SSA assumption of the AOD
444 retrieval can be increased near the critical reflectance.

445

446 **3.5. Uncertainty of AOD retrieval**

447

448 Various uncertainties result in error in AOD retrieved as the algorithm is based on a
449 single channel, where most dominant uncertainties come from estimating surface
450 reflectance and assumed aerosol model. To investigate the retrieval error, several
451 sensitivity tests were conducted. The effects of linear inversion error, assumptions of
452 BAOD, aerosol model and surface elevation were estimated in a quantitative manner
453 in addition to aerosol model error shown in Figure 6.

454 The LUT approach has been widely used to take aerosol information from satellite
455 measurement by reducing operation time. In LUT approach, the calculated value is
456 interpolated linearly from the neighboring bins for geometry, AOD, surface
457 reflectance, and elevation. Thus, the number of entries for LUT calculation must be
458 selected carefully to save operation time and maintain retrieval accuracy at the same
459 time. LUT applied in this study presents TOA reflectance calculated as a function of

460 geometrical angles of sun and satellite with 10° interval, and surface reflectance with
461 0.1 intervals. As long as the LUT approach is applied to retrieval algorithm, the linear
462 interpolation of TOA reflectance between each bin leads to the inversion error. Figure
463 7(a) and (b) show the percentage difference between retrieved and reference AODs in
464 terms of scattering angle, surface reflectance, and AOD condition. Two different
465 AODs of 0.15 and 1.20 were applied to calculate the reference reflectance with two
466 surface reflectances of 0.05 and 0.10, and solar zenith angles ranging from 0° to 57°
467 by 3° interval. The satellite zenith and azimuth angle were assumed as 10° and 40° ,
468 respectively. In Figure 7(a, b), the percentage errors increase by increasing difference
469 between the reference condition and LUT bin in terms of both scattering angle and
470 surface reflectance. The inversion error varied from 0 to 8%, which mainly increased
471 with the increase of scattering angle, and decreased with the increase of AOD. In the
472 figure, the solid lines represent the inversion error arisen solely by the angle
473 interpolation in interval of 0.1 for the surface reflectance in LUT. The dashed lines
474 representing the inversion error for the surface reflectance of 0.05 shows that the
475 assumption about linearity between bins of surface reflectance increased the error
476 negatively.

477 In the estimation of surface reflectance, the BAOD correction was applied to consider
478 continuous emission of air pollutant over East Asia. However, the BAOD estimated
479 from MODIS products contains retrieval uncertainty of the dark target algorithm. As
480 mentioned above, the expected error range of MODIS AOD is $\pm(0.05 + 15\%)$. The
481 BAOD is very low in general, and thus the expected error range can be over $\pm 100\%$
482 when the BAOD is lower than 0.05. According to a sensitivity test, the $\pm 100\%$ error
483 in the BAOD of 0.05 led to 7% error in surface reflectance of 0.05 and 11% error in
484 AOD of 0.45. The effects of BAOD error in surface reflectance and AOD are shown

485 in Figure 7(c) and (d), respectively, under the conditions of BAOD of 0.15, three
486 surface reflectance of 0.05, 0.10, and 0.15, and three AODs of 0.45, 0.80, and 1.20. In
487 general, the underestimation of the BAOD leads to the overestimation of the surface
488 reflectance. The -100 % error in the BAOD assumption caused 5.6 % overestimation
489 of surface reflectance when the surface reflectance was 0.1. Meanwhile, the 5 % error
490 in surface reflectance led to 25.56 % underestimation of the AOD when the reference
491 AOD and surface reflectance was 0.45 and 0.10, respectively. The uncertainty was
492 decreased with the increase of surface reflectance, and the sensitivity to the error in
493 surface reflectance was more significant for the low AOD condition than the high
494 AOD. In this test, the inversion error was avoided by using reference reflectance
495 calculated under the condition of LUT bins.

496 Lastly, the effect of assumption in surface elevation was analyzed, as shown in Figure
497 7(e). The assumption of surface elevation is linked with the Rayleigh scattering
498 correction. The underestimation of surface elevation leads to the overestimation of
499 atmospheric pressure, thus the over-correction of the Rayleigh scattering which
500 eventually results in the overestimation of surface reflectance, thus the
501 underestimation of the AOD. The sensitivity was tested for an elevation of 1 km, two
502 AODs of 0.15 and 0.80, and surface reflectances of 0.10. The ± 0.5 km errors in
503 surface elevation resulted in +9.63% and -10.56% errors in AOD when the reference
504 condition was assumed as the AOD of 0.15. The increasing AOD significantly
505 reduced sensitivity to the uncertainty, and ± 0.5 km error led +1.30 % and -1.43 %
506 when the AOD was 0.80. The dependence on surface reflectance and elevation were
507 not significant.

508 From the uncertainty tests, the largest uncertainty was found in the aerosol model
509 assumption by about 30 % although the effect of each uncertainty was changed by
510 condition of AOD, surface reflectance, and sun-satellite geometry.

511

512 **4. Results and validation**

513

514 **4.1. Comparison with MODIS AOD**

515

516 The greatest advantage of geostationary measurements is the availability of more
517 cloud-free observations by continuous measurements at high temporal resolution.

518 Besides, The AOD derived from geostationary satellite measurements can minimize
519 the uncertainty caused by the different and limited sampling of polar-orbiting-satellite

520 in the trend estimation (Yoon et al., 2014). Figure 8 shows examples of retrieved

521 AOD from the geostationary measurements from MI, using the single channel

522 algorithm. The RGB images, obtained from GOCI onboard the same platform

523 measured at 01:16, 02:16, 03:16, 04:16, 05:16 and 06:16 UTC on April 27, 2012,

524 show dust flow from the Shandong Peninsula to the northern Korean Peninsula.

525 Similarly, the images of retrieved AOD show values greater than 1.0 in the dust

526 plume, in contrast to the values lower than 0.4 over other regions. Compared with the

527 MODIS AOD, the retrieved AOD over dusty regions are generally higher, though the

528 distribution of MI AOD is spatially well matched over non-dusty regions. Spatially

529 averaged value of the MI AOD in dusty region [110°E-125°E, 35°N -40°N] decreased

530 steadily from 2.67 at 00 UTC to 1.69 at 07 UTC, and the minimum value of 1.43 was

531 found at 03:30 UTC. Meanwhile, the spatial mean values of AOD obtained

532 respectively from the MODIS TERRA and AQUA measurements were 1.11 at 03:55

533 UTC and 1.18 at 05:15 UTC. In the Figure 8, the AOD images of TERRA and AQUA
534 represent the measurements between 00 UTC to 05 UTC, and between 02 UTC to 06
535 UTC, respectively.

536 The results from MI also show the transport and concentration of aerosol in 30-min
537 interval, while the MODIS product can provide only two images per day. The map of
538 MI AOD in hourly intervals shows that the high concentration of aerosol was mostly
539 observed over northern China and the Yellow Sea before 0300 UTC, with the dust
540 plume extending to the East Sea across the northern Korean Peninsula. We can
541 deduce from the change in the dust plume that the wind field changed straight flow
542 from southwest to northeast in the morning to wave pattern, following a low pressure
543 system located in Manchuria. Neither the dark target algorithm of MODIS nor the
544 single channel algorithm of MI could retrieve AOD over regions of brighter surfaces,
545 due to the low sensitivity of the aerosol compared with the surface. However, unlike
546 the MI retrieval, part of the dust scene over the ocean was missed in the MODIS
547 retrieval due to sun-glint masking.

548

549 **4.2. Comparison with AERONET: DRAGON-Asia**

550

551 For quantitative validation, the retrieved AODs were compared with the measured
552 values from the 39 AERONET sun-photometer sites in Korea and Japan. To
553 investigate the effect of the new aerosol model as an input parameter to calculate the
554 LUTs, the results of the original and new AOD retrievals were compared respectively,
555 and the comparisons were shown in Figure 9. The measured AODs from all of the
556 numbered DRAGON-Asia sites listed in Table 1 were used in the comparison shown
557 in the top panel. In the lower panel, part of the AERONET AOD was used as a

558 validation group to test the consistency of the algorithm and to validate the retrieval
559 accuracy. The data from the validation group were not included in the AOP analysis
560 due to a lack of inversion datasets. The comparison results are shown in the bottom
561 panel of Figure 9. The left and right panels show evaluations of the original and new
562 AOD, respectively.

563 Using the original aerosol model, the retrieved AODs agree very well with the linear
564 regression as follows:

565

$$566 \quad \tau_{\text{MI [original LUT]}} = 1.08\tau_{\text{DRAGON-Asia}} - 0.08, \text{ RMSE} = 0.18, r = 0.87$$

567

568 Although the Pearson coefficient of 0.87 indicates a significant correlation, the
569 regression slope indicates that the retrieved AOD is overestimated by 8% compared
570 with the AERONET value. Comparison with the validation group, however, shows a
571 tendency to systematic underestimation with a slope of 1.01 and y-offset of -0.05.

572 By applying the new aerosol model, the regression slope was improved to 1.00,
573 although other measures remained similar:

574

$$575 \quad \tau_{\text{MI [new LUT]}} = 1.00\tau_{\text{DRAGON-Asia}} - 0.07, \text{ RMSE} = 0.17, r = 0.85$$

576

577 In Section 3.4, the analysis of the retrieval sensitivity to the SSA assumption showed
578 that the underestimation of the SSA in the aerosol model results in the overestimation
579 of AOD. Thus, the overestimation of the original AOD suggests that the radiative
580 absorptivity of the aerosol during MAM was slightly underestimated prior to the
581 campaign. According to Figure 6, a 1% underestimation of SSA can result in
582 overestimation of AOD by up to 7%. The uncertainty can vary with measurement

583 geometry, AOD, or surface reflectance. Therefore, to a large degree, the 8% decrease
584 in AOD can be explained by a 1.1% increase in SSA in the new aerosol model during
585 MAM. The large RMSE and the underestimation for the validation group, however,
586 are attributed to the spatial and temporal variation in AOPs, which cannot be
587 standardized by the single aerosol model. Moreover, the change of aerosol model
588 results in a decrease of percentage of the comparison data within 30% difference
589 range from 79.15% to 77.30%. In terms of the comparison of the validation group, the
590 regression slope was decreased from 1.01 to 0.93 though the comparison still shows
591 strong correlation between the retrieved and measured AOD. As long as a single
592 aerosol model is applied, the spatial and temporal variations of aerosol properties are
593 the largest uncertainty of the AOD retrieval algorithm. When the difference between
594 assumed and actual SSA become higher than 3%, the retrieval error exceed 30%. The
595 degradation of the comparison statistics shows the limitation of the single channel
596 algorithm. The uncertainties in estimation of surface reflectance and assumption of
597 linearity between LUT bins have effects on the accuracy of low AOD as described in
598 section 3.5. The sensitivity tests showed that the effects of each retrieval uncertainty
599 depend on the condition of AOD. For the condition of low AOD, the effect of aerosol
600 model assumption to the retrieval uncertainty in AOD is significantly lower than the
601 effects of surface reflectance estimation. However, insufficient number of inversion
602 data for an AOD bin between 0.0 and 0.3, where the AOD is lower than the criteria of
603 quality assurance of 0.4 (440 nm), increases the uncertainty in the assumption of
604 aerosol model for the condition of low AOD. Consequently, it was found that the
605 validation statistics for low AOD (< 0.4 at 550 nm) were significantly lower than that
606 for high AOD. While the correlation coefficient and regression slope of the low AOD
607 comparison was 0.49 and 0.35, those for high AOD condition was 0.78 and 0.86. The

608 ratio of the low AOD to the total comparison data set was 41.72%. To show the
609 retrieval accuracy for each campaign site, the Taylor diagram (Taylor, 2001) is shown
610 in Figure 10. This diagram summarizes how closely a set of retrievals matches
611 observations in terms of r , RMSE, and standard deviation. The polar angle of the
612 point from the x-axis indicates the correlation coefficient, and the radial distance
613 represents the normalized standard deviation, which in this case describes the ratio of
614 the standard deviation of the retrieved MI AOD to that of the AERONET (Yoon et al.,
615 2014) values. The distance between the symbol and the dashed arc, which represents
616 the standard deviation of the AERONET value, shows the similarity of the amplitude
617 of their variations; a radial distance of >1 indicates that the standard deviation of the
618 MI AOD is greater than that of AERONET. On the other hand, the RMSE between
619 the MI and AERONET AODs is proportional to the distance to the point on the x-axis
620 identified as “AERONET”, marked with a dotted arc. Consequently, the decrease in
621 distance between the “AERONET” point and the position of the symbol indicates an
622 increase in similarity between the retrieved and measured AODs. The normalized
623 standard deviations of retrieved AOD generally range from 1 to 1.5, except for the
624 Kohriyama (site number 12) and Matsue (site number 19) in Japan. In spite of the
625 high correlation coefficients of 0.85 and 0.78 at the sites, the high regression slopes of
626 1.58 and 1.35 suggest that the radiative absorptivity was underestimated in this region,
627 and thus the AOD was significantly overestimated in the case of high-AOD
628 conditions. The large negative y-intercepts of -0.12 and -0.25 could be caused by the
629 underestimation of AOD following an overestimation of BAOD in the case of low-
630 AOD conditions.

631 The comparison statistics of the original and new AOD, plotted in the Taylor diagram,
632 are also listed in Tables 3 and 4, respectively. The correlation coefficients obtained

633 from the 39 DRAGON sites range from 0.66 to 0.95 and the average was 0.84 when
634 the original aerosol model was applied. The maximum value was found at Anmyeon
635 (site number 3) and Kunsan_NU (National University) in Korea, and the minimum
636 value of 0.66 was found at Nishi-Harima (site number 25) in Japan. The Anmyeon
637 site was located in a rural area near ocean to monitor background condition of
638 atmosphere (e.g., Kim et al., 2007), and thus the dark surface contributes to reduce the
639 uncertainty in AOD retrieval. The Kunsan-NU site, as with the Anmyeon site, was
640 surrounded by mountain, reservoir, and rural area. Meanwhile, the Nishi-Harima site
641 was located on the top of Mount Onade (435.9 meters altitude, Nishi-Harima
642 Astronomical Observatory) among trees, and thus the uncertainty caused during
643 surface correction can be reduced, also. However, the comparison statistics showed
644 systematic underestimation of the AODs by regression slope of 0.86 and y-intercept
645 of -0.06. To compare the difference between the AOD correlations for each sites,
646 temporal variation of the AODs obtained from MI and AERONET measurements
647 were represented in Figure 11. In Figure 11, the AOD variations for the four
648 aforementioned sites were shown in order of (a) Anmyeon, (b) Kunsan_NU, (c)
649 Kohriyama, and (d) Nishi-Harima site. The red boxes and black circles, which
650 indicate the MI AOD and the AERONET value, were well matched at (a) Anmyeon
651 and (b) Kunsan-NU with good correlation statistics. The vertical distribution of
652 symbols for each day represents diurnal variation of AOD, and the variations were
653 also highly correlated regardless of time. The temporal variations showed AOD
654 increase during the period from 1 to 15 May at both sites. In other two sites in Japan,
655 Kohriyama and Nishi-Harima, any temporal pattern cannot be found because of the
656 low number of comparison data, though the variation of MI AOD was closely related
657 with the AERONET value. A notable thing in the comparison was the low number of

658 data. Table 3 showed that most of Japanese site (excepting Fukue) has lower
659 comparison data than the sites of Korean, and the low number trend was related with
660 frequency of the direct measurements of sun-photometer in Japan sites. While the
661 total number of direct AOD products in level2.0 dataset ranged between 99 and 3630
662 in Japan, the number ranged from 1296 to 5191 in Korea. The difference in data
663 counts indicates that there was frequent rain and cloud event over Japan, to result in
664 uncertainty in the AOD retrieval in the Japan including Koriyama and Nishi-Harima
665 site. However, reason of the significant underestimation trend of the MI AOD at
666 Nishi-Harima is not clear yet.

667 Excluding Fukue_2 site which has low comparison data of only 4, the regression
668 slopes at 32 AERONET sites were higher than 1.0, and the values at 9 sites exceeded
669 1.2. As well as the Kohriyama and the Matsue sites, the comparison results for all but
670 three sites (2, 30, and 32) show negative y-intercepts between -0.003 and -0.25 . As
671 with the improved correlation seen in the scatter plot, the Taylor diagram and
672 regression statistics listed in Table 4 also show improvements in retrieval accuracy at
673 each site. The distances between the data point and the “AERONET” value at each
674 site were generally reduced, especially at Tsukuba (site number 32). At this site, the
675 systematic overestimation was significantly reduced by applying the new aerosol
676 model, also leading to an improved correlation coefficient. The regression slope over
677 all sites was decreased by about 0.08, while the y-intercept was changed within a
678 range from -0.03 to 0.06 , in accordance with the increased SSA in the new aerosol
679 model. Whereas most of the comparisons were improved by the decrease in the slope,
680 some sites (11, 21, 25, 26, 28 and 36) show a better result using the original aerosol
681 model in terms of the regression slope. The change in correlation coefficient and
682 RMSE was not significant.

683

684 **5. Summary**

685

686 A single channel algorithm was used to retrieve AOD over East Asia by adopting a
687 new aerosol model, derived from data from the mesoscale network measurement
688 campaign deploying sun-sky radiometers, DRAGON-NE Asia 2012. The campaign
689 was performed during MAM 2012 to improve our understanding of the AOPs in high
690 spatial scale over well-known aerosol source regions where aerosol loading is affected
691 by both desert emissions and industrial pollutants. In addition, the direct solar
692 measurements of spectral AOD undertaken during the campaign were used to
693 improve the satellite-based aerosol retrieval algorithm by providing a dataset for
694 validation.

695 The accuracy of the single channel algorithm is strongly affected by the surface
696 reflectance estimation and the assumed aerosol model. To estimate the surface
697 reflectance, a minimum reflectance method was applied, and the BAOD was used to
698 correct for the persistent background aerosol levels over East Asia. The BAOD was
699 obtained by using the MODIS standard AOD product from 2006 to 2012. With
700 respect to aerosol model selection, however, the single channel algorithm was limited
701 by a lack of spectral information. For this reason, the aerosol model was integrated
702 from a seasonally sorted inversion dataset taking into account the monsoon climate
703 over the region, which was used to calculate LUT. To overcome the limitations of the
704 retrieval accuracy related to the limitation in aerosol type selection, it was important
705 to optimize the aerosol model. The AOPs were obtained from two AERONET
706 inversion data groups to understand the effects of assumptions in the aerosol model.

707 The original AOPs were constructed from the inversion dataset provided by 13
29

708 AERONET sites over East Asia before 2011, while the new AOPs were modified
709 using data from an increased number of measurement sites, as well as additional data
710 from the original sites. The obtained AOPs show that the denser deployment of
711 measurement sites has a greater effect on the AOPs than the extended periods of
712 measurement in terms of refractive index. The increase of effective radius of coarse
713 particle distribution as found also. This increase in spatial resolution resulted in an
714 increase of SSA by $\sim 1.1\%$ during MAM, which was expected to lead to a decrease in
715 AOD.

716 According to the sensitivity test, the error in the retrieved AOD varied from -19% to
717 $+20\%$, in proportion with the assumed SSA error of $\pm 3\%$ in the aerosol model, for a
718 scenario with reference AOD value of 0.15 and the surface reflectance of 0.05. The
719 uncertainty in retrieved AOD due to the assumed SSA error was increased at greater
720 values of AOD, and ranged between -20% and $+23\%$ when the reference AOD value
721 was 1.20. In short, the overestimation of SSA in the aerosol model results in the
722 underestimation of AOD, and assumed errors in SSA have a greater effect at higher
723 values of AOD. Considering the relationship between surface reflectance and the
724 uncertainty, the retrieval error in real measurements could be larger than the
725 suggested value when the surface reflectance is near the critical reflectance. In the
726 meantime, the error in surface reflectance shows larger effects in the accuracy of low
727 AOD than the error in SSA.

728 The qualitative comparison between AODs retrieved from MODIS and MI showed a
729 reasonably high correlation. The MI AOD showed the capability to track the dust
730 plume crossing from the Shandong Peninsula to the northern Korean Peninsula by
731 taking advantage of geostationary measurements, whereas the MODIS AOD provided
732 two AOD maps during a single day by using both Terra and Aqua. AODs retrieved

733 with both the original and new aerosol model showed a good correlation with sun-
734 photometer data from the DRAGON-Asia campaign. The correlation coefficient and
735 the RMSE were slightly changed from 0.87 to 0.85 and 0.18 to 0.17, respectively, by
736 applying the new aerosol model. Increased SSA values in the new aerosol model
737 resolved problems with AOD being overestimated, and the regression slope was
738 decreased from 1.08 to 1.00. A comparison for each campaign site also showed that
739 the statistics of the correlation were generally improved. For some regions, however,
740 changes in the aerosol model led to underestimation of the AOD.

741 As shown here, the use of a fixed aerosol model is an important issue in a single
742 channel algorithm. Similarly, the application of a well-defined model for each
743 assumed aerosol type is important to obtain accurate results from a multi-channel
744 algorithm. According to a study with the GOCI multi-channel algorithm (Choi et al.,
745 accepted), however, the effects of applying the DRAGON-Asia dataset were less
746 significant, in other words less dependent on the aerosol model assumed. The GOCI
747 algorithm categorizes 26 aerosol models according to FMF at 550 nm and SSA at 440
748 nm, and selects an optimized aerosol type at each measured pixel and time. The
749 accuracy of the BAOD is another important issue when using the minimum
750 reflectance method to retrieve AOD, because overestimation of the BAOD results in a
751 systematic underestimation of the AOD. The dense measurements of the AERONET
752 sun-photometer network can be used to optimize the BAOD at higher resolution,
753 though the network cannot cover the whole field of view of the satellite measurement.
754 Furthermore, an improved correction for cloud masking is required to reduce noise in
755 the retrieval.

756

757 **Acknowledgements**

758

759 We thank the principal investigators and their staff for establishing and maintaining
760 the AERONET sites used in this investigation. This research was supported by the
761 GEMS program of the Ministry of Environment, Korea, and the Eco Innovation
762 Program of KEITI (2012000160002). This research was partially supported by the
763 Brain Korea 21 Plus (J. Kim and M. Kim).

764

765 **References**

766

767 Bevan, S. L., North, P. R. J., Los, S. O., and Grey, W. M. F.: A global dataset of
768 atmospheric aerosol optical depth and surface reflectance from AATSR,
769 Remote Sens Environ, 116, 199-210, 10.1016/j.rse.2011.05.024, 2012.

770 Castanho, A. D. D. A., Martins, J. V., and Artaxo, P.: MODIS aerosol optical depth
771 Retrievals with high spatial resolution over an urban area using the critical
772 reflectance, J Geophys Res-Atmos, 113, Artn D02201 Doi
773 10.1029/2007jd008751, 2008.

774 Choi, M., Kim, J., Lee, j., Kim, M., Park, Y.-J., Jeong, U., Kim, W., Holben, B., Eck,
775 T.F., Lim, J. H., and Song, C. K.: GOCI Yonsei Aerosol Retrieval (YAER)
776 Algorithm and Validation During DRAGON-NE Asia 2012 Campaign,
777 Atmos. Meas. Tech. Discuss., accepted, 2015

778 Deroubaix, A., Martiny, N., Chiapello, I., and Marticorena, B.: Suitability of OMI
779 aerosol index to reflect mineral dust surface conditions: Preliminary
780 application for studying the link with meningitis epidemics in the sahel,
781 Remote Sens Environ, 133, 116-127, DOI 10.1016/j.rse.2013.02.009, 2013.

782 Dubovik, O., and King, M. D.: A flexible inversion algorithm for retrieval of aerosol
783 optical properties from Sun and sky radiance measurements, *J Geophys*
784 *Res-Atmos*, 105, 20673-20696, Doi 10.1029/2000jd900282, 2000.

785 Dubovik, O., Smirnov, A., Holben, B. N., King, M. D., Kaufman, Y. J., Eck, T. F.,
786 and Slutsker, I.: Accuracy assessments of aerosol optical properties
787 retrieved from Aerosol Robotic Network (AERONET) Sun and sky
788 radiance measurements, *J Geophys Res-Atmos*, 105, 9791-9806, Doi
789 10.1029/2000jd900040, 2000.

790 Dubovik, O., Holben, B., Eck, T. F., Smirnov, A., Kaufman, Y. J., King, M. D., Tanre,
791 D., and Slutsker, I.: Variability of absorption and optical properties of key
792 aerosol types observed in worldwide locations, *J Atmos Sci*, 59, 590-608,
793 Doi 10.1175/1520-0469(2002)059<0590:Voaap>2.0.Co;2, 2002.

794 Eck, T. F., Holben, B. N., Reid, J. S., Dubovik, O., Smirnov, A., O'Neill, N. T.,
795 Slutsker, I., and Kinne, S.: Wavelength dependence of the optical depth of
796 biomass burning, urban, and desert dust aerosols, *J Geophys Res-Atmos*,
797 104, 31333-31349, Doi 10.1029/1999jd900923, 1999.

798 Fraser, R. S., and Kaufman, Y. J.: The relative importance of aerosol scattering and
799 absorption in remote-sensing, *IEEE T Geosci Remote*, 23, 625-633, Doi
800 10.1109/Tgrs.1985.289380, 1985.

801 Frey, R. A., Ackerman, S. A., Liu, Y. H., Strabala, K. I., Zhang, H., Key, J. R., and
802 Wang, X. G.: Cloud detection with MODIS. Part I: Improvements in the
803 MODIS cloud mask for collection 5, *J Atmos Ocean Tech*, 25, 1057-1072,
804 10.1175/2008jtecha1052.1, 2008.

805 Grey, W. M. F., North, P. R. J., Los, S. O., and Mitchell, R. M.: Aerosol optical depth
806 and land surface reflectance from Multiangle AATSR measurements:

807 Global validation and intersensor comparisons, *Ieee T Geosci Remote*, 44,
808 2184-2197, 10.1109/Tgrs.2006.872079, 2006.

809 Holben, B. N., Eck, T. F., Slutsker, I., Tanre, D., Buis, J. P., Setzer, A., Vermote, E.,
810 Reagan, J. A., Kaufman, Y. J., Nakajima, T., Lavenu, F., Jankowiak, I., and
811 Smirnov, A.: Aeronet - a federated instrument network and data archive for
812 aerosol characterization, *Remote Sens Environ*, 66, 1-16, Doi
813 10.1016/S0034-4257(98)00031-5, 1998.

814 Holben, B. N., Tanre, D., Smirnov, A., Eck, T. F., Slutsker, I., Abuhassan, N.,
815 Newcomb, W. W., Schafer, J. S., Chatenet, B., Lavenu, F., Kaufman, Y. J.,
816 Castle, J. V., Setzer, A., Markham, B., Clark, D., Frouin, R., Halthore, R.,
817 Karneli, A., O'Neill, N. T., Pietras, C., Pinker, R. T., Voss, K., and Zibordi,
818 G.: An emerging ground-based aerosol climatology: Aerosol optical depth
819 from AERONET, *J Geophys Res-Atmos*, 106, 12067-12097, Doi
820 10.1029/2001jd900014, 2001.

821 Hsu, N. C., Tsay, S. C., King, M. D., and Herman, J. R.: Aerosol properties over
822 bright-reflecting source regions, *IEEE T Geosci Remote*, 42, 557-569, Doi
823 10.1109/Tgrs.2004.824067, 2004.

824 Huebert, B. J., Bates, T., Russell, P. B., Shi, G. Y., Kim, Y. J., Kawamura, K.,
825 Carmichael, G., and Nakajima, T.: An overview of ACE-Asia: Strategies
826 for quantifying the relationships between Asian aerosols and their climatic
827 impacts, *J Geophys Res-Atmos*, 108, Artn 8633

828 Kahn, R. A., Gaitley, B. J., Garay, M. J., Diner, D. J., Eck, T. F., Smirnov, A., and
829 Holben, B. N.: Multiangle Imaging SpectroRadiometer global aerosol
830 product assessment by comparison with the Aerosol Robotic Network, *J
831 Geophys Res-Atmos*, 115, Artn D2320910.1029/2010jd014601, 2010.

832 Kim, J., Lee, J., Lee, H. C., Higurashi, A., Takemura, T., and Song, C. H.:
833 Consistency of the aerosol type classification from satellite remote sensing
834 during the atmospheric brown cloud-east Asia regional experiment
835 campaign, *J Geophys Res-Atmos*, 112, Artn D22s33Doi
836 10.1029/2006jd008201, 2007.

837 Kim, J., Yoon, J. M., Ahn, M. H., Sohn, B. J., and Lim, H. S.: Retrieving aerosol
838 optical depth using visible and mid-IR channels from geostationary satellite
839 MTSAT-1R, *Int J Remote Sens*, 29, 6181-6192, Doi
840 10.1080/01431160802175553, 2008.

841 Kim, M., Kim, J., Wong, M. S., Yoon, J., Lee, J., Wu, D., Chan, P. W., Nichol, J. E.,
842 Chung, C.-Y. C., and Ou, M.-L.: Improvement of aerosol optical depth
843 retrieval over Hong Kong from a geostationary meteorological satellite
844 using critical reflectance with background optical depth correction, *Remote
845 Sens Environ*, 142, 176-187, 2014.

846 Knapp, K. R., Vonder Haar, T. H., and Kaufman, Y. J.: Aerosol optical depth retrieval
847 from goes-8: Uncertainty study and retrieval validation over South America,
848 *J Geophys Res-Atmos*, 107, Artn 4055Doi 10.1029/2001jd000505, 2002.

849 Knapp, K. R., Frouin, R., Kondragunta, S., and Prados, A.: Toward aerosol optical
850 depth retrievals over land from GOES visible radiances: Determining
851 surface reflectance, *Int J Remote Sens*, 26, 4097-4116, Doi
852 10.1080/0143116050500099329, 2005.

853 Kotchenova, S. Y., Vermote, E. F., Matarrese, R., and Klemm, F. J.: Validation of a
854 vector version of the 6S radiative transfer code for atmospheric correction
855 of satellite data. Part i: Path radiance, *Applied optics*, 45, 6762-6774, Doi
856 10.1364/Ao.45.006762, 2006.

857 Kotchenova, S. Y., and Vermote, E. F.: Validation of a vector version of the 6S
858 radiative transfer code for atmospheric correction of satellite data. Part ii.
859 Homogeneous Lambertian and anisotropic surfaces, *Applied optics*, 46,
860 4455-4464, Doi 10.1364/Ao.46.004455, 2007.

861 Lee, J., Kim, J., Song, C. H., Kim, S. B., Chun, Y., Sohn, B. J., and Holben, B. N.:
862 Characteristics of aerosol types from AERONET sunphotometer
863 measurements, *Atmos Environ*, 44, 3110-3117, DOI
864 10.1016/j.atmosenv.2010.05.035, 2010a.

865 Lee, J., Kim, J., Song, C. H., Ryu, J. H., Ahn, Y. H., and Song, C. K.: Algorithm for
866 retrieval of aerosol optical properties over the ocean from the Geostationary
867 Ocean Color Imager, *Remote Sens Environ*, 114, 1077-1088, DOI
868 10.1016/j.rse.2009.12.021, 2010b.

869 Lee, J., Kim, J., Yang, P., and Hsu, N. C.: Improvement of aerosol optical depth
870 retrieval from MODIS spectral reflectance over the global ocean using new
871 aerosol models archived from AERONET inversion data and tri-axial
872 ellipsoidal dust database, *Atmos Chem Phys*, 12, 7087-7102, DOI
873 10.5194/acp-12-7087-2012, 2012.

874 Levy, R. C., Remer, L. A., and Dubovik, O.: Global aerosol optical properties and
875 application to Moderate Resolution Imaging Spectroradiometer aerosol
876 retrieval over land, *J Geophys Res-Atmos*, 112, Artn
877 D1321010.1029/2006jd007815, 2007a.

878 Levy, R. C., Remer, L. A., Mattoo, S., Vermote, E. F., and Kaufman, Y. J.: Second-
879 generation operational algorithm: Retrieval of aerosol properties over land
880 from inversion of Moderate Resolution Imaging Spectroradiometer spectral

881 reflectance, *J Geophys Res-Atmos*, 112, Artn D13211Doi
882 10.1029/2006jd007811, 2007b.

883 Levy, R. C., Remer, L. A., Kleidman, R. G., Mattoo, S., Ichoku, C., Kahn, R., and
884 Eck, T. F.: Global evaluation of the collection 5 MODIS dark-target aerosol
885 products over land, *Atmos Chem Phys*, 10, 10399-10420, DOI
886 10.5194/acp-10-10399-2010, 2010.

887 Levy, R. C., Mattoo, S., Munchak, L. A., Remer, L. A., Sayer, A. M., Patadia, F., and
888 Hsu, N. C.: The Collection 6 MODIS aerosol products over land and ocean,
889 *Atmos Meas Tech*, 6, 2989-3034, 10.5194/amt-6-2989-2013, 2013.

890 Lyapustin, A., Smirnov, A., Holben, B., Chin, M., Streets, D. G., Lu, Z., Kahn, R.,
891 Slutsker, I., Laszlo, I., Kondragunta, S., Tanre, D., Dubovik, O., Goloub, P.,
892 Chen, H. B., Sinyuk, A., Wang, Y., and Korkin, S.: Reduction of aerosol
893 absorption in Beijing since 2007 from MODIS and AERONET, *Geophys*
894 *Res Lett*, 38, Artn L10803 Doi 10.1029/2011gl047306, 2011a.

895 Lyapustin, A., Wang, Y., Laszlo, I., Kahn, R., Korkin, S., Remer, L., Levy, R., and
896 Reid, J. S.: Multiangle implementation of atmospheric correction (MAIAC):
897 2. Aerosol algorithm, *J Geophys Res-Atmos*, 116, Artn D03211Doi
898 10.1029/2010jd014986, 2011b.

899 Nakajima, T., Yoon, S. C., Ramanathan, V., Shi, G. Y., Takemura, T., Higurashi, A.,
900 Takamura, T., Aoki, K., Sohn, B. J., Kim, S. W., Tsuruta, H., Sugimoto, N.,
901 Shimizu, A., Tanimoto, H., Sawa, Y., Lin, N. H., Lee, C. T., Goto, D., and
902 Schutgens, N.: Overview of the Atmospheric Brown Cloud East Asian
903 Regional Experiment 2005 and a study of the aerosol direct radiative
904 forcing in east Asia, *J Geophys Res-Atmos*, 112, Artn D24s91

905 Park, M. E., Song, C. H., Park, R. S., Lee, J., Kim, J., Lee, S., Woo, J. H., Carmichael,
906 G. R., Eck, T. F., Holben, B. N., Lee, S. S., Song, C. K., and Hong, Y. D.:
907 New approach to monitor transboundary particulate pollution over
908 Northeast Asia, *Atmos Chem Phys*, 14, 659-674, 10.5194/acp-14-659-2014,
909 2014.

910 Pope, C. A., and Dockery, D. W.: Health effects of fine particulate air pollution: Lines
911 that connect, *J Air Waste Manage*, 56, 709-742, 2006.

912 Remer, L. A., Kaufman, Y. J., Tanre, D., Mattoo, S., Chu, D. A., Martins, J. V., Li, R.
913 R., Ichoku, C., Levy, R. C., Kleidman, R. G., Eck, T. F., Vermote, E., and
914 Holben, B. N.: The MODIS aerosol algorithm, products, and validation, *J*
915 *Atmos Sci*, 62, 947-973, Doi 10.1175/Jas3385.1, 2005.

916 Saide, P. E., Kim, J., Song, C. H., Choi, M., Cheng, Y. F., and Carmichael, G. R.:
917 Assimilation of next generation geostationary aerosol optical depth
918 retrievals to improve air quality simulations, *Geophys Res Lett*, 41, 9188-
919 9196, 10.1002/2014gl062089, 2014

920 Sayer, A. M., Hsu, N. C., Bettenhausen, C., Jeong, M. J., Holben, B. N., and Zhang, J.:
921 Global and regional evaluation of over-land spectral aerosol optical depth
922 retrievals from SeaWiFS, *Atmos Meas Tech*, 5, 1761-1778, 10.5194/amt-5-
923 1761-2012, 2012.

924 Sayer, A. M., Hsu, N. C., Eck, T. F., Smirnov, A., and Holben, B. N.: AERONET-
925 based models of smoke-dominated aerosol near source regions and
926 transported over oceans, and implications for satellite retrievals of aerosol
927 optical depth, *Atmos Chem Phys*, 14, 11493-11523, 10.5194/acp-14-11493-
928 2014, 2014.

929 Smirnov, A., Holben, B. N., Eck, T. F., Dubovik, O., and Slutsker, I.: Cloud-
930 screening and quality control algorithms for the AERONET database,
931 Remote Sens Environ, 73, 337-349, Doi 10.1016/S0034-4257(00)00109-7,
932 2000.

933 Stocker, T. F., Qin, D., Plattner, G.-K., Tignor, M., Allen, S. K., Boschung, J., Nauels,
934 A., Xia, Y., Bex, V., and Midgley, P. M.: Climate change 2013: The
935 physical science basis, Intergovernmental Panel on Climate Change,
936 Working Group I Contribution to the IPCC Fifth Assessment Report
937 (AR5)(Cambridge Univ Press, New York), 2013.

938 Taylor, K. E.: Summarizing multiple aspects of model performance in a single
939 diagram., J Geophys Res-Atmos, 106, 7183-7192, Doi
940 10.1029/2000jd900719, 2001.

941 Torres, O., Tanskanen, A., Veihelmann, B., Ahn, C., Braak, R., Bhartia, P. K.,
942 Veefkind, P., and Levelt, P.: Aerosols and surface UV products from ozone
943 monitoring instrument observations: An overview, J Geophys Res-Atmos,
944 112, Artn D24s47Doi 10.1029/2007jd008809, 2007.

945 Urm, Y. D., and Sohn, B. J.: Estimation of aerosol optical thickness over East Asia
946 using GMS-5 visible channel measurements, J. of Atmosphere, 15, 203-211,
947 2005.Vermote, E. F., Tanre, D., Deuze, J. L., Herman, M., and Morcrette, J.
948 J.: Second simulation of the satellite signal in the solar spectrum, 6S: An
949 overview, IEEE T Geosci Remote, 35, 675-686, Doi 10.1109/36.581987,
950 1997.

951 von Hoyningen-Huene, W., Yoon, J., Vountas, M., Istomina, L. G., Rohen, G., Dinter,
952 T., Kokhanovsky, A. A., and Burrows, J. P.: Retrieval of spectral aerosol

953 optical thickness over land using ocean color sensors MERIS and SeaWiFS,
954 Atmos Meas Tech, 4, 151-171, DOI 10.5194/amt-4-151-2011, 2011.

955 Wang, J., Christopher, S. A., Brechtel, F., Kim, J., Schmid, B., Redemann, J., Russell,
956 P. B., Quinn, P., and Holben, B. N.: Geostationary satellite retrievals of
957 aerosol optical thickness during ACE-Asia, J Geophys Res-Atmos, 108,
958 Artn 8657Doi 10.1029/2003jd003580, 2003.

959 Waquet, F., Cairns, B., Knobelspiesse, K., Chowdhary, J., Travis, L. D., Schmid, B.,
960 and Mishchenko, M. I.: Polarimetric remote sensing of aerosols over land, J
961 Geophys Res-Atmos, 114, Artn D0120610.1029/2008jd010619, 2009.

962 Wong, M. S., Lee, K. H., Nichol, J. E., and Li, Z. Q.: Retrieval of aerosol optical
963 thickness using MODIS 500 x 500 m(2), a study in Hong Kong and the
964 pearl river delta region, IEEE T Geosci Remote, 48, 3318-3327, Doi
965 10.1109/Tgrs.2010.2045124, 2010.

966 Yang, P., Feng, Q., Hong, G., Kattawar, G. W., Wiscombe, W. J., Mishchenko, M. I.,
967 Dubovik, O., Laszlo, I., and Sokolik, I. N.: Modeling of the scattering and
968 radiative properties of nonspherical dust-like aerosols, J Aerosol Sci, 38,
969 995-1014, DOI 10.1016/j.jacros.2007.07.001, 2007.

970 Yoon, J.-M.: Effects of atmospheric and surface properties on the retrieval of AOD
971 from geostationary satellite, PH.D. thesis, Department of Atmospheric
972 Sciences, Yonsei Univ, Seoul, Republic of Korea, 2006.

973 Yoon, J. M., Kim, J., Lee, J. H., Cho, H. K., Sohn, B. J., and Ahn, M. A.: Retrieved of
974 aerosol optical depth over East Asia from a geostationary satellite,
975 MTSAT-1R, Asia-Pacific J. Atmos. Sci., 43, 133-142, 2007.

976 Yoon, J., Burrows, J. P., Vountas, M., von Hoyningen-Huene, W., Chang, D. Y.,
977 Richter, A., and Hilboll, A.: Changes in atmospheric aerosol loading

978 retrieved from space-based measurements during the past decade, Atmos
979 Chem Phys, 14, 6881-6902, DOI 10.5194/acp-14-6881-2014, 2014.

980 Zhang, H., Lyapustin, A., Wang, Y., Kondragunta, S., Laszlo, I., Ciren, P., and Hoff,
981 R. M.: A multi-angle aerosol optical depth retrieval algorithm for
982 geostationary satellite data over the United States, Atmos Chem Phys, 11,
983 11977-11991, DOI 10.5194/acp-11-11977-2011, 2011.

984 Zhang, J. L., Christopher, S. A., and Holben, B. N.: Intercomparison of smoke aerosol
985 optical thickness derived from GOES 8 imager and ground-based sun
986 photometers, J Geophys Res-Atmos, 106, 7387-7397, Doi
987 10.1029/2000jd900540, 2001.

988

989 **List of Tables**

990

991 Table 1. Summary of AERONET sites used in this study. Columns “Period” represent
992 the retrieval period of the daily inversion product (level 2.0), and the
993 longitude (long., °E) and latitude (lat., °N) show the location for each site.
994 The number in front of the site name lists the sites operated for the
995 DRAGON-Asia campaign, where “D” is the initial of the campaign. The
996 numbers are linked to Table 4, Table 5, and Figure 9. The color and type of
997 character categorizes the inversion dataset into the "original", "new", and
998 "excepted" groups. While the "original" group is compiled from the
999 inversion datasets obtained before 2011 at sites in grey cell, the "new"
1000 group consists of the total dataset excluding the "excepted" group shown in
1001 bold and italic type.

1002 Table 2. Integrated AOPs at each AOD bin (550 nm) from AERONET inversion data.
1003 Each of the AOD bins ranges between 0.0-0.3, 0.3-0.6, 0.6-1.0, 1.0-1.4,
1004 1.4-1.8, and 1.8-3.0, respectively, and the median value is shown in the
1005 Table. The values in (a) (upper panel) were obtained from the original
1006 inversion data group, and those in the middle and lower panels (b and c)
1007 were estimated from temporally and temporal-spatially extended datasets,
1008 respectively.

1009 Table 3. Summary statistics of the comparison between the MI AOD [550 nm]
1010 retrieved with the original LUT and AERONET AOD [550 nm]. The site
1011 numbers correspond to the number listed in Table 1 and Figure 10(a). The
1012 sites mentioned in section 4.2 are represented by grey shade.

1013 Table 4. Summary statistics of the comparison between the MI AOD [550 nm]
1014 retrieved with the updated LUT and AERONET AOD [550 nm]. The site
1015 numbers correspond to the number listed in Table 1 and Figure 10(b). The
1016 sites mentioned in section 4.2 are represented by grey shade.
1017
1018

1019 **List of Figures**

1020

1021 Figure 1. Location and number of data points of the AERONET sun-photometers
1022 deployed during DRAGON-NE Asia 2012. The color of each symbol
1023 represents the number of AOD [level 2.0] data points measured for the
1024 campaign.

1025 Figure 2. The (a, c) average and (b, d) standard deviation (1σ) of (a, b) AOD at 500
1026 nm and (c, d) Ångström Exponent between 440 nm and 870 nm during
1027 DRAGON-NE Asia 2012 campaign for each site

1028 Figure 3. Flowchart of a single channel algorithm for AOD retrieval, adapted from
1029 Kim et al. (2014).

1030 Figure 4. Absolute minimum AOD at 550 nm obtained from MODIS level 2.0
1031 products (MYD04_Lv2.0) from 2006 to 2012 at $0.25^\circ \times 0.25^\circ$ resolution.

1032 Figure 5. Volume size distribution for each AOD bins, as obtained from the original
1033 and new AERONET inversion data listed in Table 1. The effective radius
1034 and standard deviation of the fine and coarse mode particles are described
1035 in Table 2. The size distributions are averaged for each AOD interval, and
1036 the color of the curve indicates the mean AOD value.

1037 Figure 6. Dependence of the AOD retrieval error on error in assumed SSA for four
1038 different AOD cases. The SSA error represents the percentage difference
1039 between SSAs used to the simulation and the retrieval, and the AOD error
1040 indicates the difference between the retrieved AOD and a reference value.
1041 Surface reflectance is assumed to be 0.05, and scattering angles ranging
1042 from 135.73° to 173.23° are applied. The error bars indicate the standard

1043 deviation of AOD error obtained from the geometric variation, and the
1044 numbers in parentheses are the SSA error without the inversion error.

1045 Figure 7. Uncertainties in retrieval of AOD and surface reflectance; (a), (b) AOD
1046 error depending on scattering angle for two cases of AOD [0.15, 1.20] and
1047 two cases surface reflectance [0.05, 0.10]; (c) error in surface reflectance
1048 according to BAOD assumption error for three conditions of BAOD [0.05,
1049 0.10, 0.15]; and (d) sensitivity of AOD error to error in surface reflectance
1050 and elevation for each assumed condition of AOD.

1051 Figure 8. RGB images obtained from GOCI measurement and examples of retrieved
1052 AOD from MI measurement on April 27, 2012. Two panels at left bottom
1053 side are the MODIS AOD product obtained from TERRA (MOD04) and
1054 AQUA (MYD04) measurements. The AOD ranges between 0 and 2 in
1055 those panels.

1056 Figure 9. Evaluation of the AOD retrieved from MI measurements during DRAGON-
1057 Asia. The x-axis and y-axis indicate the values of AOD at 550 nm obtained
1058 from AERONET and MI measurements, respectively, and the color of the
1059 symbols shows the data counts for each AOD bin. The y-axis on the left [(a)
1060 and (c)] and right side [(b) and (d)] represents the AOD retrieved using the
1061 original and new LUT, respectively. The plots on the top [(a) and (b)]
1062 contain the data measured from all campaign sites, whereas those on the
1063 bottom [(c) and (d)] contain only the values from the sites excluded in the
1064 AOP analysis. The linear regression line with a Pearson coefficient (r) and
1065 root mean square error (RMSE) were included for each plot.

1066 Figure 10. Taylor diagrams comparing the retrieved AODs and the values obtained
1067 from AERONET sun-photometer measurements during the DRAGON-

1068 2012 campaign. (a): Comparison of results from the original AOD, (b):
1069 comparison of results from the new AOD. The numbers above each symbol
1070 indicate the number of the DRAGON-Asia site, as listed in Table 1.

1071 Figure 11. Temporal variations of AODs during the DRAGON-Asia. The red box and
1072 black circle represent the values retrieved from MI and AERONET
1073 measurement, respectively, and each panel shows the time series for
1074 different AERONET sites; (a) Anmyeon, (b) Kunsan_NU, (c) Kohriyama,
1075 (d) Nishiharima.

1076

1077 Table 1. Summary of AERONET sites used in this study. Columns “Period” represent the retrieval
1078 period of the daily inversion product (level 2.0), and the longitude (long., °E) and latitude (lat., °N)
1079 show the location for each site. The number in front of the site name lists the sites operated for the
1080 DRAGON-Asia campaign, where “D” is the initial of the campaign. The numbers are linked to Table
1081 4, Table 5, and Figure 9. The color and type of character categorizes the inversion dataset into the
1082 "original", "new", and "excepted" groups. While the "original" group is compiled from the inversion
1083 datasets obtained before 2011 at sites in grey cell, the "new" group consists of the total dataset
1084 excluding the "excepted" group shown in bold and italic type.

1085

Site	Long.	Lat.	Period	Site	Long.	Lat.	Period
(1) Baengnyeong	124.63	37.97	2010-2013	<u>(36) Osaka</u>	<u>135.59</u>	<u>34.65</u>	<u>2001-2013</u>
(2) Chiba_University	140.1	35.63	2011-2012	(37) Seoul_SNU	126.95	37.46	2000-2013
(3) D_Anmyeon	126.33	36.54	DRAGON2012*	<u>(38) Shirahama</u>	<u>135.36</u>	<u>33.69</u>	<u>2000-2013</u>
(4) D_Bokjeong	127.13	37.46	DRAGON2012	(39) Yonsei_University	126.93	37.56	2011-2013
(5) D_Fukue	128.68	32.75	DRAGON2012	Anmyon	126.33	36.54	1999-2007
(6) D_Fukue_2	128.82	32.67	DRAGON2012	Bac_Giang	106.23	21.29	2003-2009
(7) D_Fukuoka	130.48	33.52	DRAGON2012	Bach_Long_Vy	107.73	20.13	2010-2011
(8) D_GangneungWNU	128.87	37.77	DRAGON2012	Beijing	<u>116.38</u>	<u>39.98</u>	<u>2001-2013</u>
(9) D_Guwol	126.72	37.45	DRAGON2012	<u>Chen-Kung Univ</u>	<u>120.22</u>	<u>23</u>	<u>2002-2012</u>
(10) D_Hankuk_UFS	127.27	37.34	DRAGON2012	<u>Dongsha Island</u>	<u>116.73</u>	<u>20.7</u>	<u>2004-2013</u>
(11) D_Kobe	135.29	34.72	DRAGON2012	<u>EPA-NCU</u>	<u>121.19</u>	<u>24.97</u>	<u>2006-2013</u>
(12) D_Kohriyama	140.38	37.36	DRAGON2012	Hangzhou-ZFU	119.73	30.26	2007-2007
(13) D_Kongju_NU	127.14	36.47	DRAGON2012	Hefei	117.16	31.91	2005-2008
(14) D_Konkuk_Univ	127.08	37.54	DRAGON2012	<u>Hong Kong Hok Tsui</u>	<u>14.26</u>	<u>22.21</u>	<u>2007-2010</u>
(15) D_Korea_Univ	127.03	37.58	DRAGON2012	<u>Hong Kong PolyU</u>	<u>114.18</u>	<u>22.3</u>	<u>2005-2013</u>
(16) D_Kunsan_NU	126.68	35.94	DRAGON2012	<u>Inner Mongolia</u>	<u>115.95</u>	<u>42.68</u>	<u>2001-2001</u>
(17) D_Kyoto	135.78	35.03	DRAGON2012	Jingtai	104.1	37.33	2008-2008
(18) D_Kyungil_Univ	128.82	36.07	DRAGON2012	Lanzhou_City	103.85	36.05	2009-2010
(19) D_Matsue	133.01	35.48	DRAGON2012	Liangning	122.7	41.51	2005-2005
(20) D_Mokpo_NU	126.44	34.91	DRAGON2012	Luang_Namtha	101.42	20.93	2012-2014
(21) D_Mt_Ikoma	135.68	34.68	DRAGON2012	<u>Lulin</u>	<u>120.87</u>	<u>23.47</u>	<u>2007-2014</u>
(22) D_Mt_Rokko	135.23	34.76	DRAGON2012	Minqin	102.96	38.61	2010-2010
(23) D_NIER	126.64	37.57	DRAGON2012	NGHIA_DO	105.8	21.05	2010-2013
(24) D_Nara	135.83	34.69	DRAGON2012	PKU_PEK	116.18	39.59	2006-2008
(25) D_Nishiharima	134.34	35.03	DRAGON2012	SACOL	104.14	35.95	2006-2012
(26) D_Osaka-North	135.51	34.77	DRAGON2012	Shouxian	116.78	32.56	2008-2008
(27) D_Osaka-South	135.5	34.54	DRAGON2012	<u>Taichung</u>	<u>120.49</u>	<u>24.11</u>	<u>2005-2005</u>
(28) D_Pusan_NU	129.08	35.24	DRAGON2012	Taihu	120.22	31.42	2005-2012
(29) D_Sanggye	127.07	37.66	DRAGON2012	<u>Taipei CWB</u>	<u>121.5</u>	<u>25.03</u>	<u>2002-2013</u>
(30) D_Sinjeong	126.86	37.52	DRAGON2012	<u>Ussuriysk</u>	<u>132.16</u>	<u>43.7</u>	<u>2004-2013</u>
(31) D_Soha	126.89	37.45	DRAGON2012	XiangHe	116.96	39.75	2001-2012
(32) D_Tsukuba	140.12	36.05	DRAGON2012	Xinglong	117.58	40.4	2006-2012
<u>(33) Gosan_SNU</u>	<u>126.16</u>	<u>33.29</u>	<u>2001-2013</u>	Yufa_PEK	116.18	39.31	2006-2006
<u>(34) Gwangju_GIST</u>	<u>126.84</u>	<u>35.23</u>	<u>2004-2012</u>	Zhangye	100.28	39.08	2008-2008
(35) Noto	137.14	37.33	2001-2013				

1087 *DRAGON2012 : Period of DRADON-Asia 2012 campaign [March –May, 2012]

1089 Table 2. Integrated AOPs for each AOD bin (550 nm) from AERONET inversion data. Each of the
 1090 AOD bins ranges between 0.0-0.3, 0.3-0.6, 0.6-1.0, 1.0-1.4, 1.4-1.8, and 1.8-3.0, respectively, and
 1091 the median value is shown in the Table. The values in (a) (upper panel) were obtained from the
 1092 original inversion data group, and those in the middle and lower panels (b and c) were estimated
 1093 from temporally and temporal-spatially extended datasets, respectively.

(a) Original Aerosol Model	AOD					
	0.15	0.45	0.8	1.2	1.6	>2.6
SSA at 675 nm	0.911	0.921	0.928	0.932	0.939	0.945
Refractive index [Real] at 675 nm(STD)	1.47(0.06)	1.47(0.05)	1.47(0.05)	1.49(0.05)	1.53(0.05)	1.52(0.06)
Refractive index [Im.] at 675 nm(STD)	0.0085 (0.0046)	0.0075 (0.0050)	0.0077 (0.0049)	0.0075 (0.0044)	0.0060 (0.0041)	0.0050 (0.0032)
Effective Radius-F (μm)	0.14	0.15	0.18	0.19	0.18	0.20
Effective Radius-C (μm)	1.76	1.90	2.08	2.16	2.01	2.03
Standard deviation-F	0.45	0.47	0.51	0.54	0.55	0.56
Standard deviation-C	0.69	0.64	0.62	0.58	0.54	0.52
Number of data	55	528	270	87	26	21
(b) Updated Aerosol Model (temporally extended)	AOD					
	0.15	0.45	0.8	1.2	1.6	>2.6
SSA at 675 nm	0.910	0.923	0.932	0.935	0.940	0.949
Refractive index [Real] at 675 nm(STD)	1.48(0.06)	1.47(0.05)	1.48(0.05)	1.49(0.05)	1.52(0.05)	1.51(0.05)
Refractive index [Im.] at 675 nm(STD)	0.0083 (0.0049)	0.0072 (0.0086)	0.0071 (0.0047)	0.0070 (0.0044)	0.0059 (0.0036)	0.0048 (0.0031)
Effective Radius-F (μm)	0.14	0.15	0.17	0.18	0.18	0.20
Effective Radius-C (μm)	1.84	1.94	2.09	2.16	2.02	2.01
Standard deviation-F	0.45	0.47	0.51	0.54	0.53	0.56
Standard deviation-C	0.69	0.64	0.61	0.58	0.55	0.53
Number of data	75	677	370	112	37	31
(c) Updated Aerosol Model (temporal-spatially extended)	AOD					
	0.15	0.45	0.8	1.2	1.6	>2.6
SSA at 675 nm	0.916	0.927	0.935	0.940	0.944	0.951
Refractive index [Real] at 675 nm(STD)	1.48(0.06)	1.48(0.05)	1.48(0.05)	1.50(0.05)	1.51(0.05)	1.51(0.05)
Refractive index [Im.] at 675 nm(STD)	0.0073 (0.0043)	0.0065 (0.0072)	0.0061 (0.0041)	0.0060 (0.0040)	0.0054 (0.0039)	0.0046 (0.0037)
Effective Radius-F (μm)	0.14	0.15	0.16	0.17	0.17	0.20
Effective Radius-C (μm)	1.87	1.95	2.07	2.11	2.05	1.98
Standard deviation-F	0.46	0.48	0.51	0.55	0.57	0.56
Standard deviation-C	0.69	0.65	0.61	0.58	0.55	0.54
Number of data	219	1431	767	235	74	51

1094 Table 3. Summary statistics of the comparison between the MI AOD [550 nm] retrieved with the

1095 original LUT and AERONET AOD [550 nm]. The site numbers correspond to the number listed in
 1096 Table 1 and Figure 9(a). The sites mentioned in section 4.2 are represented by grey shade.

Site No.	datan	MI AOD mean(STD)	DRAGON AOD mean(STD)	AOD Diff.	R	slope	y-offset	RMSE
1	400	0.42(0.34)	0.43(0.25)	-0.010	0.942	1.278	-0.13	0.115
2	76	0.43(0.21)	0.36(0.16)	0.071	0.814	1.054	0.051	0.122
3	273	0.51(0.39)	0.55(0.31)	-0.033	0.949	1.190	-0.138	0.121
4	341	0.63(0.34)	0.66(0.26)	-0.023	0.829	1.101	-0.089	0.192
5	408	0.52(0.37)	0.70(0.36)	-0.172	0.891	0.915	-0.112	0.167
6	4	0.61(0.17)	0.68(0.02)	-0.067	0.927	7.337	-4.359	0.056
7	109	0.36(0.24)	0.41(0.17)	-0.049	0.859	1.198	-0.130	0.122
8	182	0.46(0.22)	0.50(0.18)	-0.044	0.771	0.955	-0.021	0.141
9	458	0.56(0.35)	0.55(0.26)	0.004	0.871	1.164	-0.087	0.169
10	275	0.57(0.32)	0.59(0.26)	-0.019	0.875	1.077	-0.065	0.156
11	108	0.45(0.27)	0.51(0.22)	-0.062	0.782	0.966	-0.045	0.165
12	23	0.58(0.29)	0.45(0.16)	0.138	0.849	1.581	-0.122	0.152
13	232	0.67(0.47)	0.68(0.37)	-0.012	0.914	1.154	-0.117	0.190
14	355	0.58(0.35)	0.64(0.27)	-0.065	0.862	1.118	-0.140	0.179
15	430	0.60(0.35)	0.66(0.27)	-0.063	0.846	1.102	-0.130	0.189
16	227	0.70(0.50)	0.67(0.44)	0.031	0.952	1.104	-0.039	0.153
17	47	0.49(0.31)	0.54(0.21)	-0.047	0.778	1.111	-0.107	0.190
18	272	0.43(0.27)	0.49(0.21)	-0.066	0.812	1.051	-0.091	0.159
19	56	0.60(0.28)	0.64(0.16)	-0.035	0.776	1.345	-0.254	0.173
20	254	0.66(0.32)	0.60(0.26)	0.058	0.890	1.090	0.003	0.147
21	71	0.41(0.21)	0.42(0.18)	-0.009	0.834	0.987	-0.003	0.117
22	112	0.44(0.21)	0.41(0.14)	0.035	0.775	1.199	-0.047	0.132
23	206	0.66(0.37)	0.58(0.25)	0.081	0.892	1.336	-0.114	0.167
24	82	0.37(0.26)	0.45(0.20)	-0.086	0.907	1.185	-0.170	0.107
25	46	0.30(0.21)	0.42(0.16)	-0.120	0.656	0.862	-0.062	0.159
26	69	0.40(0.23)	0.48(0.22)	-0.087	0.858	0.925	-0.050	0.119
27	138	0.49(0.32)	0.51(0.21)	-0.029	0.778	1.162	-0.112	0.197
28	317	0.48(0.29)	0.55(0.25)	-0.063	0.871	1.006	-0.067	0.143
29	336	0.62(0.38)	0.67(0.29)	-0.054	0.835	1.080	-0.108	0.206
30	246	0.62(0.40)	0.63(0.27)	-0.009	0.868	1.259	-0.171	0.197
31	437	0.60(0.35)	0.61(0.26)	-0.015	0.821	1.104	-0.078	0.200
32	135	0.50(0.27)	0.35(0.17)	0.144	0.703	1.152	0.090	0.194
33	458	0.56(0.39)	0.62(0.33)	-0.051	0.942	1.099	-0.112	0.130
34	290	0.63(0.38)	0.63(0.27)	0.004	0.913	1.274	-0.169	0.156
35	93	0.41(0.24)	0.43(0.17)	-0.017	0.935	1.303	-0.147	0.086
36	115	0.43(0.29)	0.51(0.20)	-0.087	0.787	1.140	-0.159	0.178
37	260	0.61(0.35)	0.61(0.27)	-0.001	0.835	1.097	-0.060	0.194
38	92	0.32(0.20)	0.38(0.14)	-0.055	0.804	1.136	-0.107	0.121
39	316	0.64(0.37)	0.65(0.26)	-0.018	0.805	1.140	-0.110	0.219

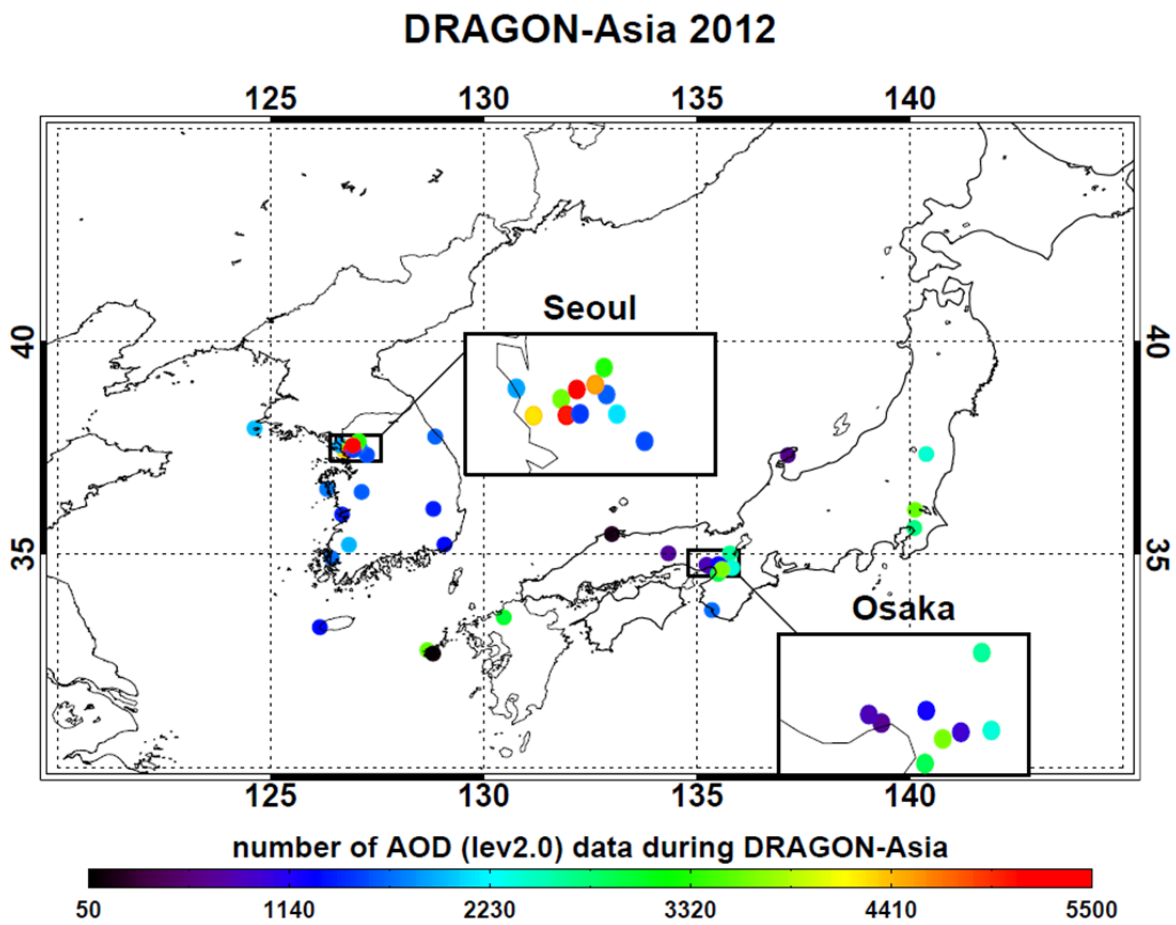
1097
 1098 Table 4. Summary statistics of the comparison between the MI AOD [550 nm] retrieved with the
 50

1099 updated LUT and AERONET AOD [550 nm]. The site numbers correspond to the number listed in
 1100 Table 1 and Figure 9(a). The sites mentioned in section 4.2 are represented by grey shade.

Site No.	datan	MI AOD mean(STD)	DRAGON AOD mean(STD)	AOD Diff.	R	slope	y-offset	RMSE
1	402	0.39(0.32)	0.43(0.25)	-0.033	0.944	1.205	-0.121	0.107
2	76	0.40(0.19)	0.36(0.16)	0.045	0.812	0.965	0.058	0.112
3	284	0.49(0.39)	0.55(0.32)	-0.058	0.949	1.139	-0.134	0.122
4	340	0.58(0.31)	0.66(0.26)	-0.072	0.803	0.974	-0.055	0.185
5	413	0.50(0.35)	0.69(0.36)	-0.195	0.882	0.856	-0.095	0.164
6	4	0.58(0.16)	0.68(0.02)	-0.097	0.926	6.857	-4.062	0.053
7	108	0.34(0.22)	0.41(0.17)	-0.064	0.853	1.113	-0.110	0.116
8	186	0.44(0.21)	0.50(0.18)	-0.066	0.763	0.894	-0.013	0.136
9	454	0.51(0.32)	0.55(0.26)	-0.038	0.847	1.036	-0.057	0.167
10	276	0.53(0.30)	0.59(0.26)	-0.065	0.854	0.973	-0.049	0.155
11	111	0.41(0.25)	0.50(0.21)	-0.087	0.775	0.896	-0.035	0.155
12	22	0.56(0.28)	0.45(0.16)	0.103	0.854	1.537	-0.141	0.143
13	242	0.62(0.44)	0.68(0.37)	-0.056	0.902	1.073	-0.106	0.190
14	353	0.53(0.33)	0.64(0.27)	-0.111	0.842	1.014	-0.120	0.176
15	431	0.56(0.33)	0.66(0.27)	-0.108	0.830	1.019	-0.120	0.186
16	234	0.64(0.46)	0.66(0.42)	-0.013	0.949	1.040	-0.039	0.147
17	44	0.43(0.24)	0.52(0.21)	-0.088	0.805	0.928	-0.050	0.139
18	276	0.40(0.26)	0.49(0.21)	-0.092	0.787	0.979	-0.081	0.157
19	56	0.59(0.28)	0.64(0.16)	-0.054	0.745	1.290	-0.240	0.183
20	261	0.60(0.29)	0.59(0.26)	0.005	0.880	0.984	0.015	0.138
21	71	0.38(0.20)	0.42(0.18)	-0.036	0.832	0.919	-0.002	0.111
22	111	0.41(0.19)	0.41(0.13)	0.006	0.765	1.087	-0.029	0.123
23	208	0.62(0.35)	0.58(0.26)	0.034	0.885	1.179	-0.070	0.164
24	82	0.34(0.23)	0.45(0.19)	-0.104	0.895	1.098	-0.148	0.104
25	46	0.29(0.20)	0.42(0.16)	-0.134	0.652	0.802	-0.051	0.150
26	70	0.38(0.23)	0.49(0.22)	-0.104	0.835	0.882	-0.047	0.125
27	137	0.46(0.31)	0.52(0.21)	-0.058	0.774	1.112	-0.116	0.194
28	315	0.45(0.26)	0.54(0.25)	-0.097	0.852	0.900	-0.042	0.136
29	338	0.57(0.36)	0.67(0.29)	-0.098	0.816	0.997	-0.096	0.206
30	245	0.57(0.37)	0.63(0.27)	-0.058	0.842	1.129	-0.138	0.197
31	440	0.55(0.33)	0.61(0.27)	-0.060	0.798	0.997	-0.058	0.201
32	138	0.46(0.25)	0.35(0.17)	0.104	0.710	1.080	0.075	0.179
33	460	0.53(0.37)	0.61(0.33)	-0.080	0.938	1.042	-0.106	0.128
34	294	0.59(0.37)	0.64(0.28)	-0.048	0.917	1.181	-0.163	0.146
35	93	0.40(0.24)	0.43(0.18)	-0.033	0.936	1.227	-0.132	0.082
36	117	0.42(0.31)	0.52(0.20)	-0.104	0.770	1.171	-0.193	0.197
37	261	0.56(0.33)	0.61(0.27)	-0.051	0.803	0.977	-0.036	0.194
38	94	0.30(0.19)	0.37(0.15)	-0.066	0.799	1.037	-0.079	0.113
39	318	0.59(0.35)	0.65(0.26)	-0.066	0.786	1.042	-0.093	0.217

1101

1102

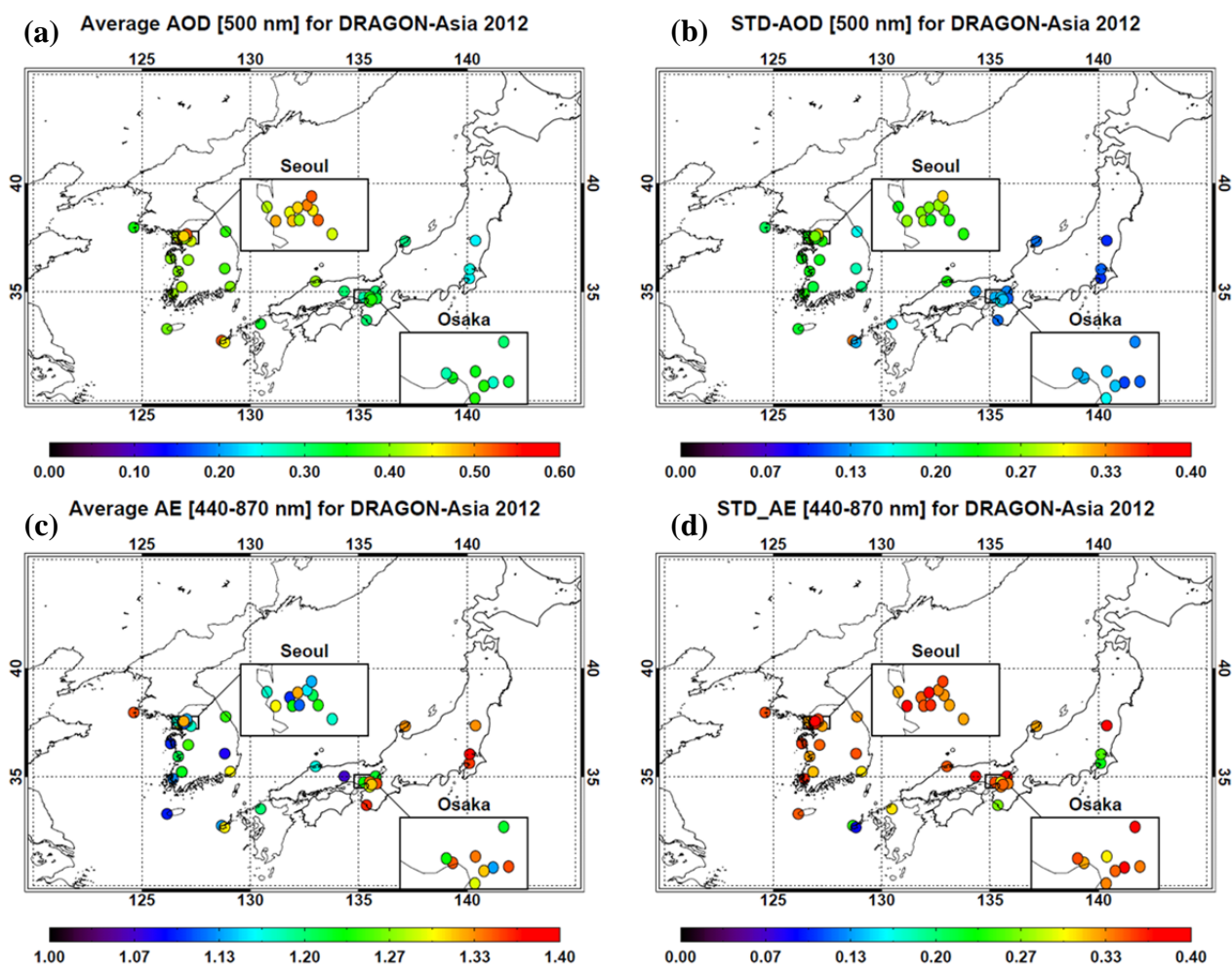


1103

1104 Figure 1. Location and number of data points of the AERONET sun-photometers deployed during
1105 DRAGON-NE Asia 2012. The color of each symbol represents the number of AOD [level 2.0] data
1106 points measured for the campaign.

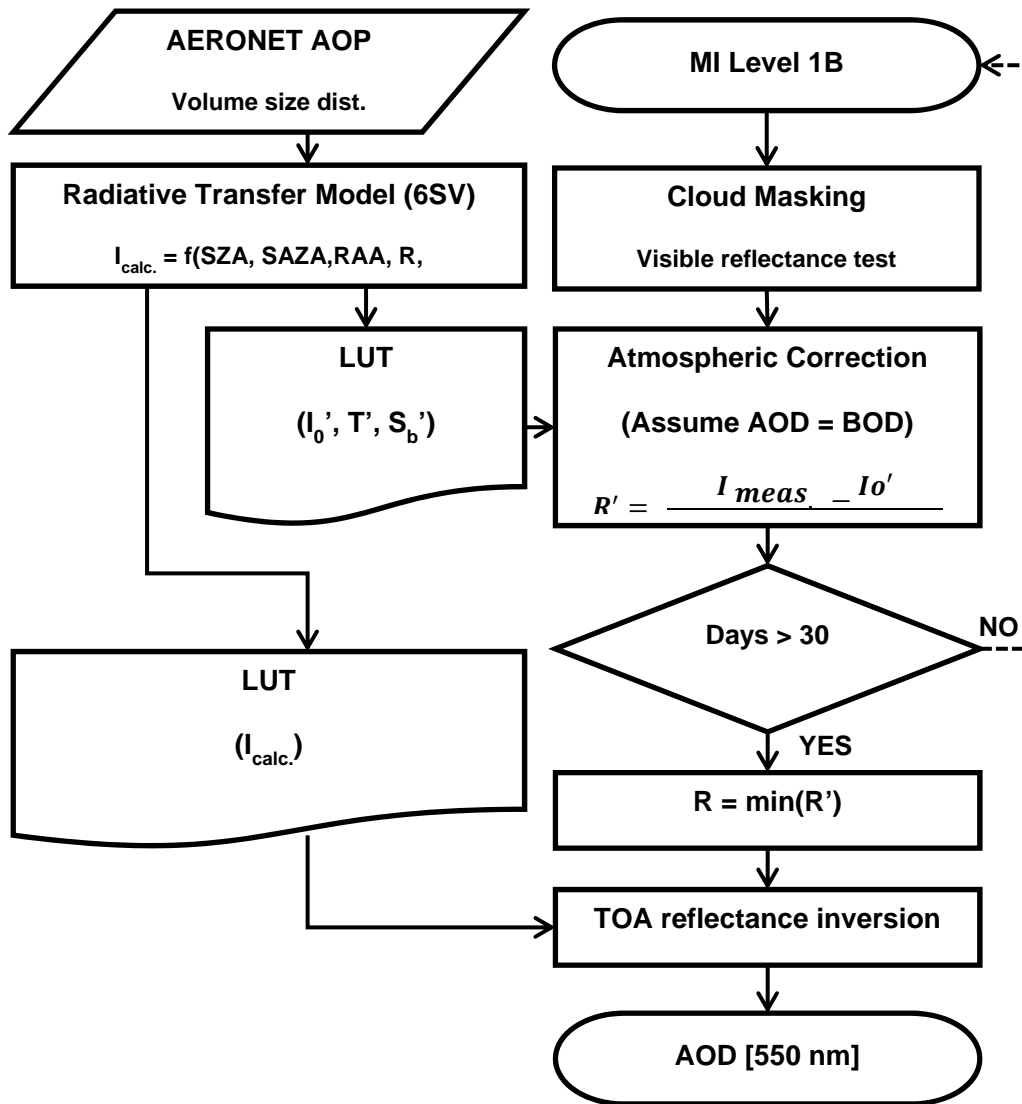
1107

1108



1109

1110 Figure 2. The (a, c) average and (b, d) standard deviation (1σ) of (a, b) AOD at 500 nm and (c, d)
 1111 Ångström Exponent between 440 nm and 870 nm during DRAGON-NE Asia 2012 campaign for
 1112 each site



1113

1114

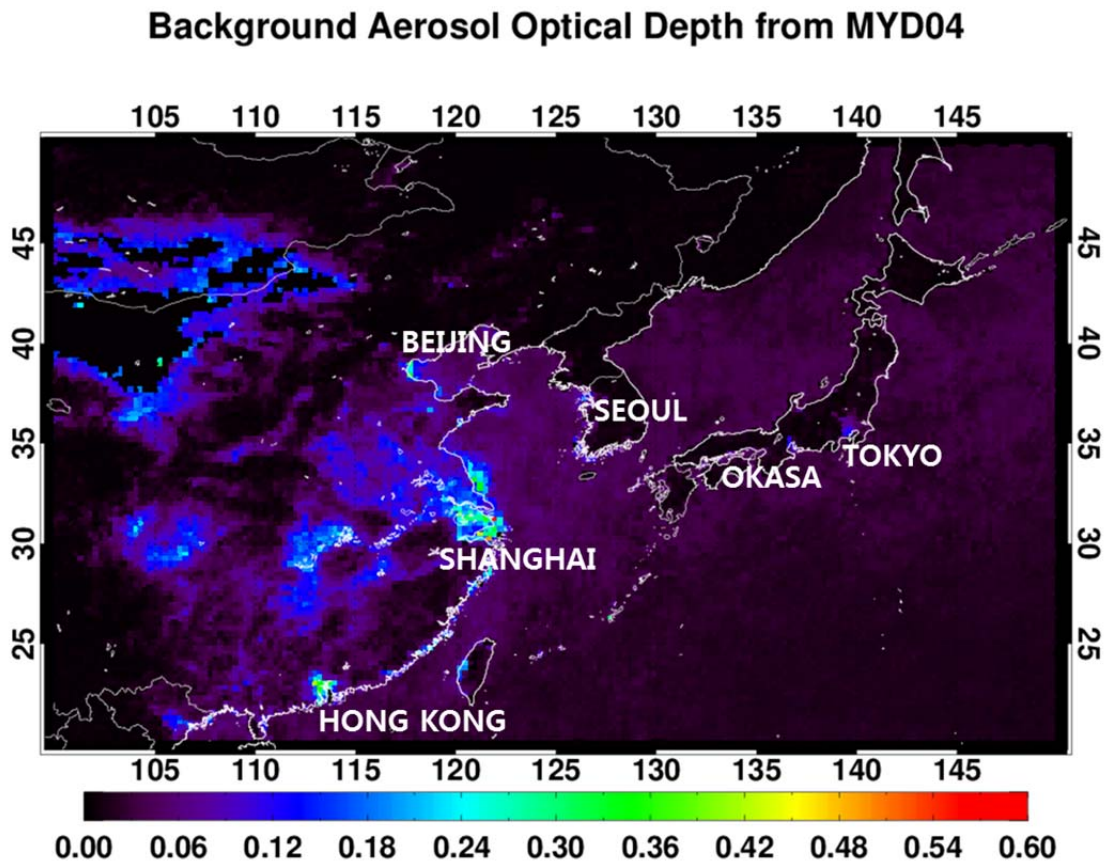
1115 Figure 3. Flowchart of a single channel algorithm for AOD retrieval, adapted from Kim et al. (2014).

1116

1117

1118

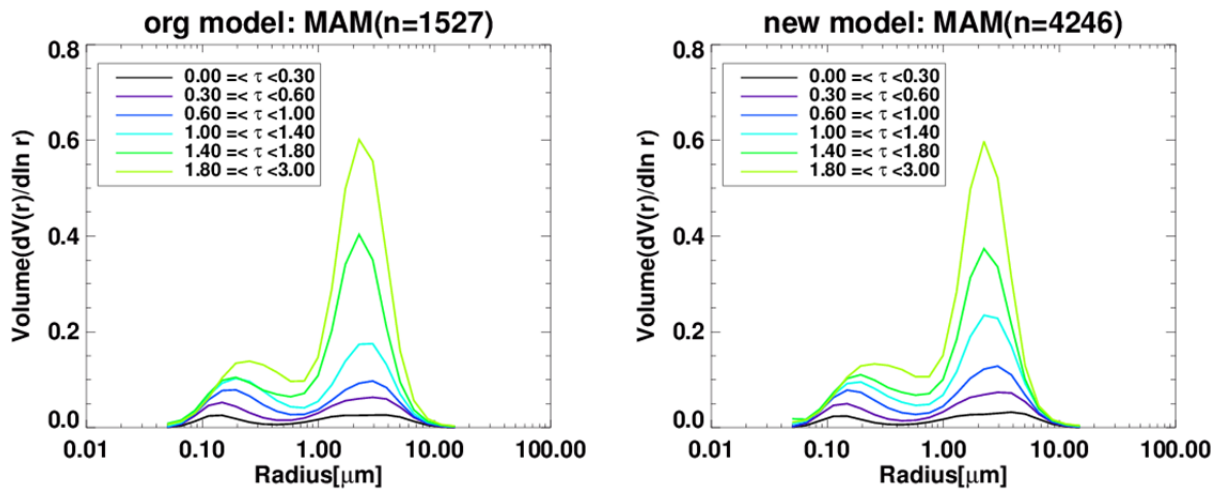
1119



1120

1121 Figure 4. Absolute minimum AOD at 550 nm obtained from MODIS level 2.0 products
1122 (MYD04_Lv2.0) from 2006 to 2012 at $0.25^\circ \times 0.25^\circ$ resolution.

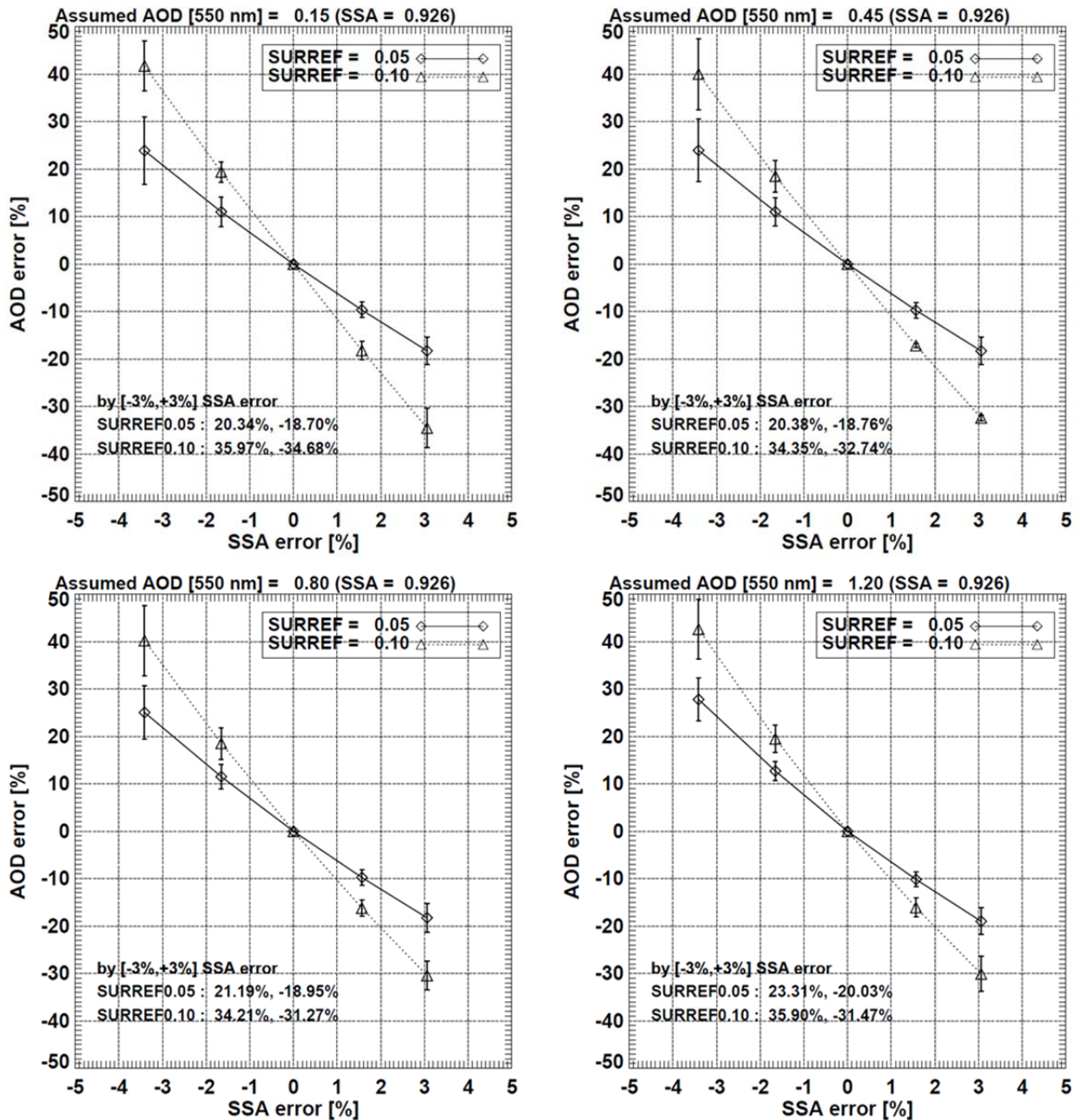
1123



1124

1125 Figure 5. Volume size distribution for each AOD bins, as obtained from the original and new
 1126 AERONET inversion data listed in Table 1. The effective radius and standard deviation of the fine
 1127 and coarse mode particles are described in Table 2. The size distributions are averaged for each AOD
 1128 interval, and the color of the curve indicates the mean AOD value.

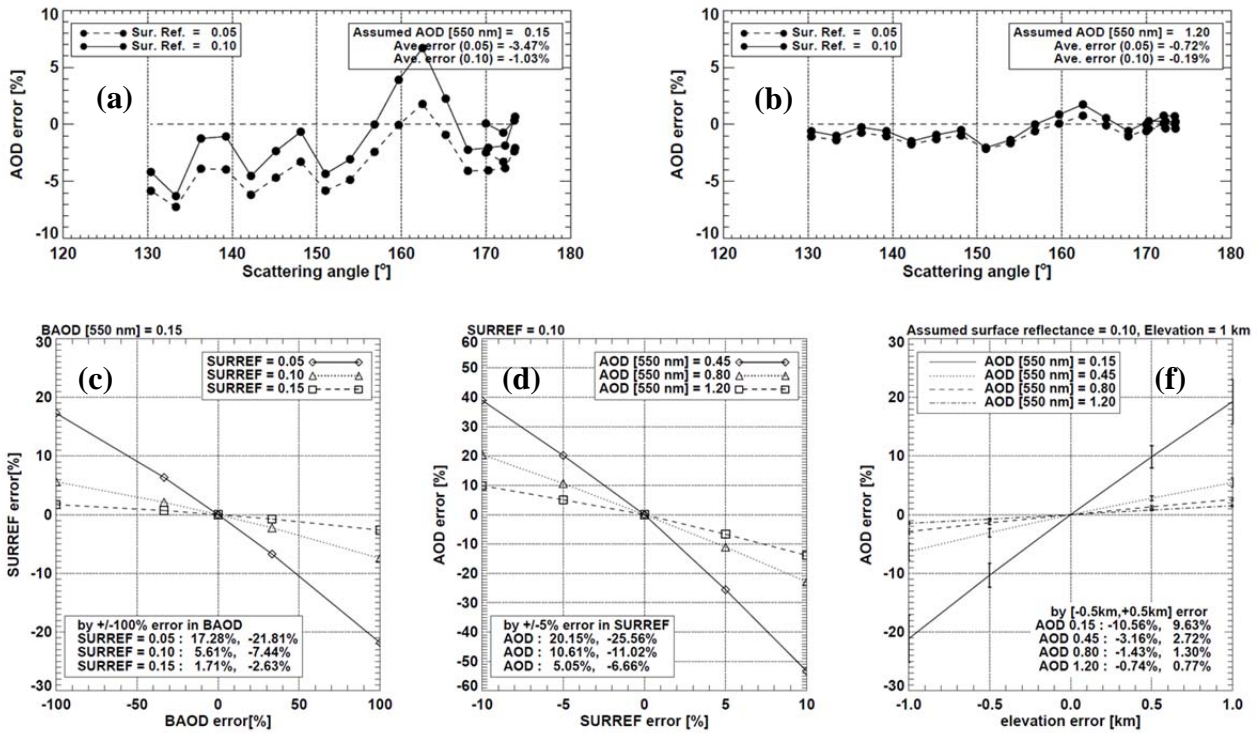
1129



1130

1131 Figure 6. Dependence of the AOD retrieval error on error in assumed SSA for four different AOD
 1132 cases. The SSA error represents the percentage difference between SSAs used to the simulation and
 1133 the retrieval, and the AOD error indicates the difference between the retrieved AOD and a reference
 1134 value. Surface reflectance is assumed to be 0.05, and scattering angles ranging from 135.73° to
 1135 173.23° are applied. The error bars indicate the standard deviation of AOD error obtained from the
 1136 geometric variation, and the numbers in parentheses are the SSA error without the inversion error.

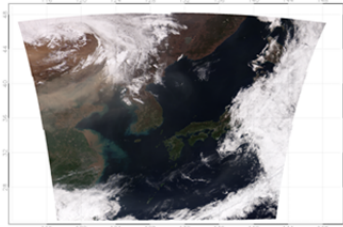
1137



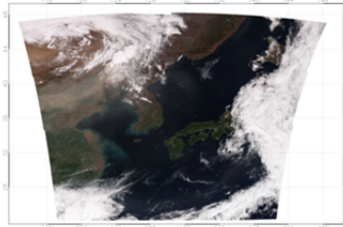
1138

1139 Figure 7. Uncertainties in retrieval of AOD and surface reflectance; (a), (b) AOD error depending on
 1140 scattering angle for two cases of AOD [0.15, 1.20] and two cases surface reflectance [0.05, 0.10]; (c)
 1141 error in surface reflectance according to BAOD assumption error for three conditions of BAOD
 1142 [0.05, 0.10, 0.15]; and (d) sensitivity of AOD error to error in surface reflectance and elevation for
 1143 each assumed condition of AOD.
 1144

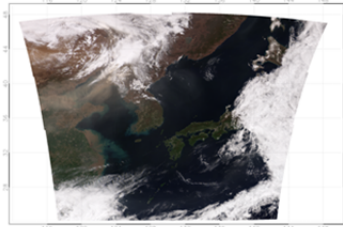
GOCI RGB 20120427 01:16



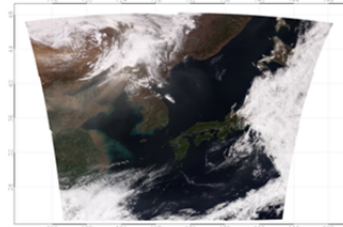
GOCI RGB 20120427 02:16



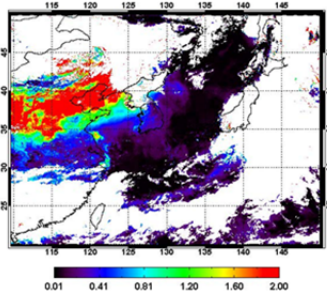
GOCI RGB 20120427 03:16



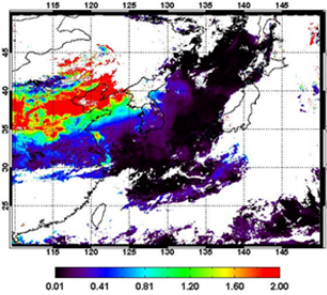
GOCI RGB 20120427 04:16



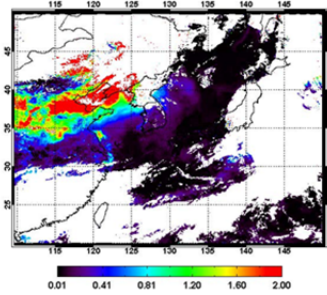
MI AOD 20120427 01:15



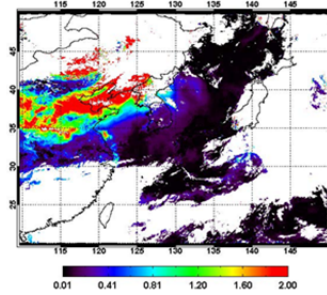
MI AOD 20120427 02:00



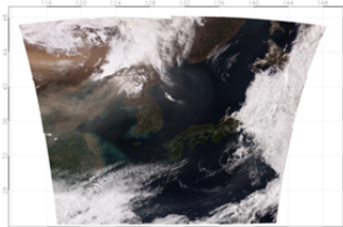
MI AOD 20120427 03:15



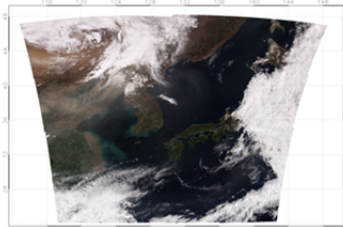
MI AOD 20120427 04:15



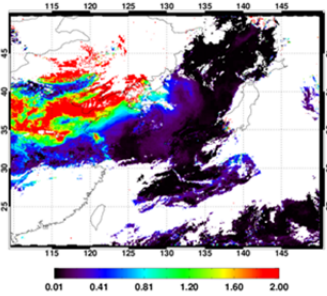
GOCI RGB 20120427 05:16



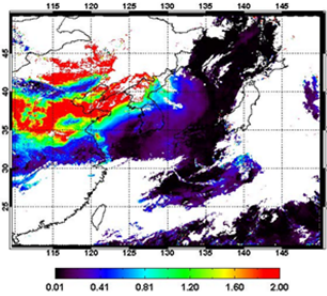
GOCI RGB 20120427 06:16



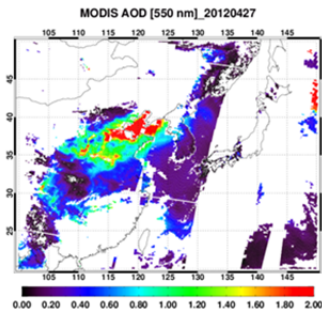
MI AOD 20120427 05:00



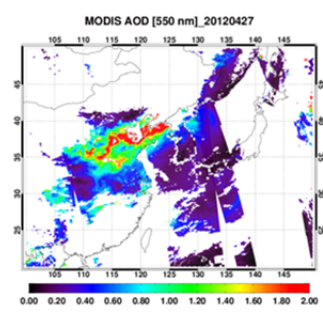
MI AOD 20120427 06:15



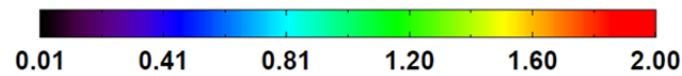
MOD AOD 20120427
00 - 05 UTC



MYD AOD 20120427
02 - 06 UTC

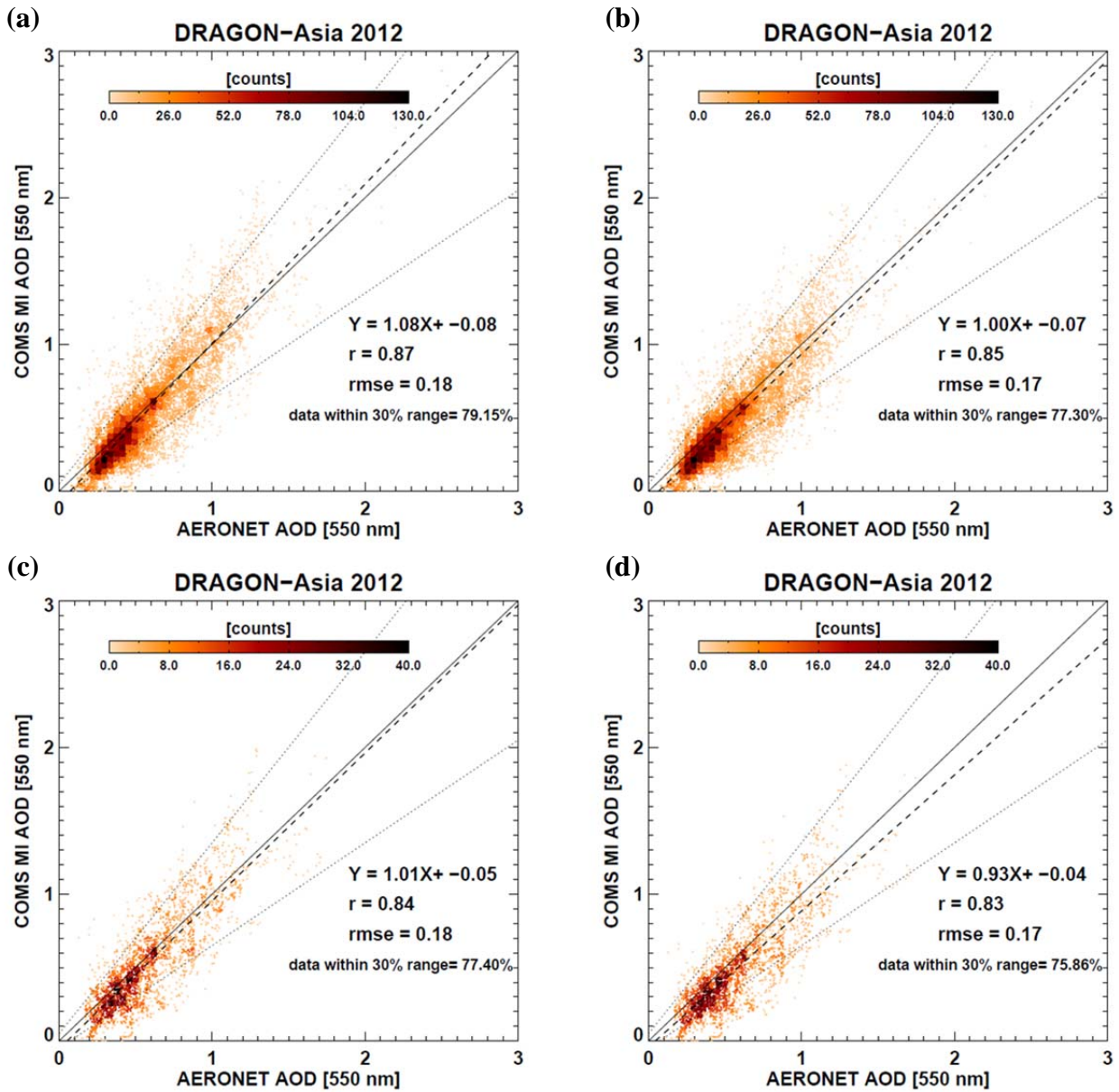


AOD [550 nm]



1146 Figure 8. RGB images obtained from GOCI measurement and examples of retrieved AOD from MI measurement on April 27, 2012. Two panels
1147 at left bottom side are the MODIS AOD product obtained from TERRA (MOD04) and AQUA (MYD04) measurements. The AOD ranges
1148 between 0 and 2 in those panels.

1149

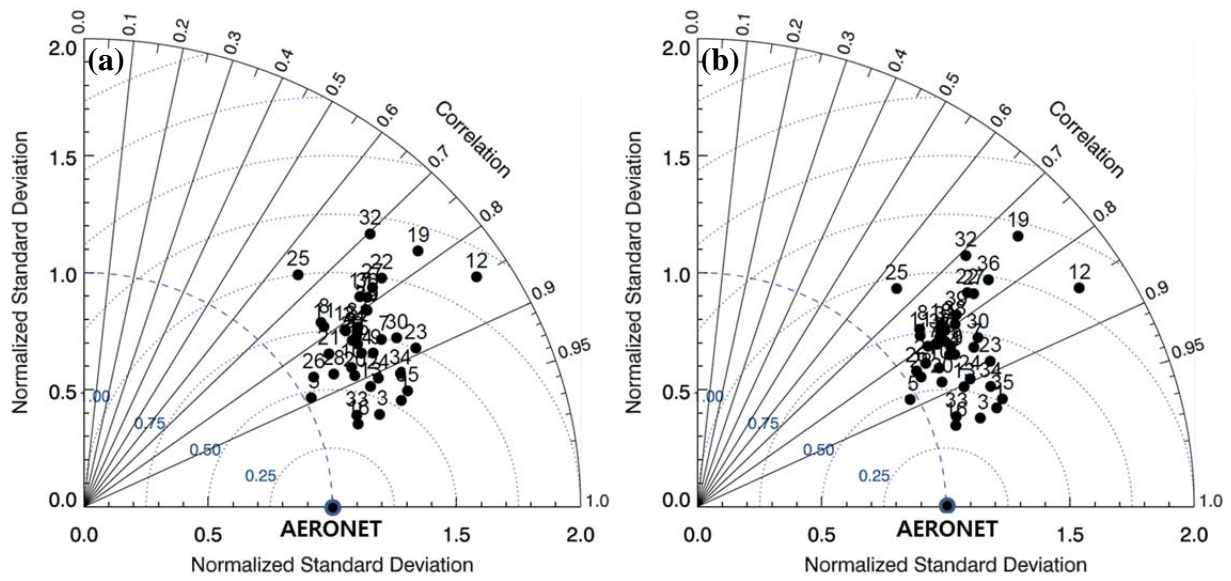


1151

1152 Figure 9. Evaluation of the AOD retrieved from MI measurements during DRAGON-Asia. The x-
 1153 axis and y-axis indicate the values of AOD at 550 nm obtained from AERONET and MI
 1154 measurements, respectively, and the color of the symbols shows the data counts for each AOD bin.
 1155 The y-axis on the left [(a) and (c)] and right side [(b) and (d)] represents the AOD retrieved using the
 1156 original and new LUT, respectively. The plots on the top [(a) and (b)] contain the data measured from
 1157 all campaign sites, whereas those on the bottom [(c) and (d)] contain only the values from the sites
 1158 excluded in the AOP analysis. The linear regression line with a Pearson coefficient (r) and root mean
 1159 square error (RMSE) were included for each plot.

1160

1161

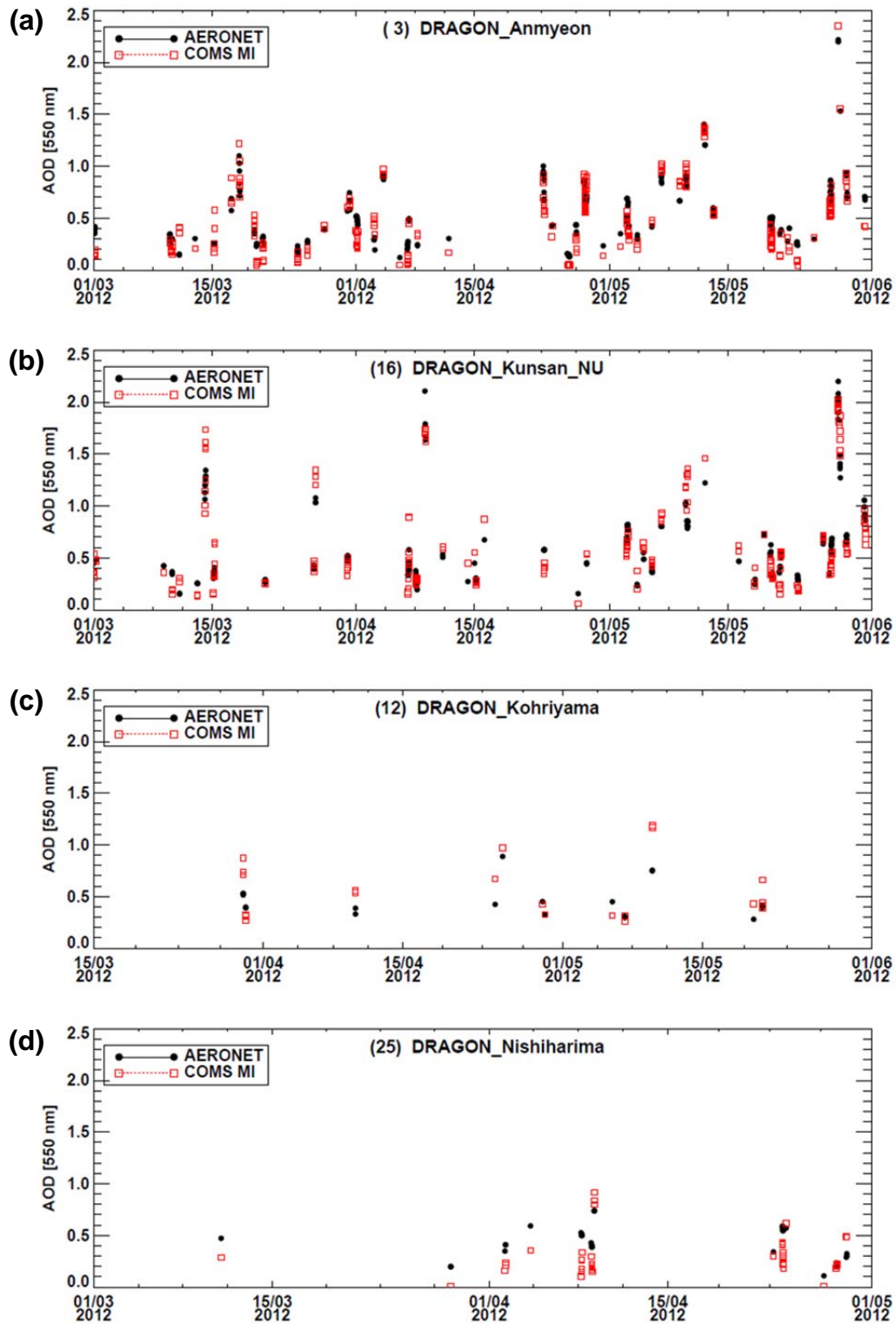


1162

1163

1164 Figure 10. Taylor diagrams comparing the retrieved AODs and the values obtained from AERONET
1165 sun-photometer measurements during the DRAGON-2012 campaign. (a): Comparison of results
1166 from the original AOD, (b): comparison of results from the new AOD. The numbers above each
1167 symbol indicate the number of the DRAGON-Asia site, as listed in Table 1.

1168



1169

1170 Figure 11. Temporal variations of AODs during the DRAGON-Asia. The red box and black circle
 1171 represent the values retrieved from MI and AERONET measurement, respectively, and each panel
 1172 shows the time series for different AERONET sites; (a) Anmyeon, (b) Kunsan_NU, (c) Kohriyama,
 1173 (d) Nishiharima.

1174